Article

Imaging quantum oscillations and millitesla pseudomagnetic fields in graphene

https://doi.org/10.1038/s41586-023-06763-5

Received: 1 July 2023

Accepted: 19 October 2023

Published online: 22 November 2023

Open access

Check for updates

Haibiao Zhou[1,5], Nadav Auerbach[1,5], Matan Uzan[1,5], Yaozhang Zhou[1], Nasrin Banu[1], Weifeng Zhi[1], Martin E. Huber[2], Kenji Watanabe[3], Takashi Taniguchi[4], Yuri Myasoedov[1], Binghai Yan[1] & Eli Zeldov[1]✉

The exceptional control of the electronic energy bands in atomically thin quantum materials has led to the discovery of several emergent phenomena[1]. However, at present there is no versatile method for mapping the local band structure in advanced two-dimensional materials devices in which the active layer is commonly embedded in the insulating layers and metallic gates. Using a scanning superconducting quantum interference device, here we image the de Haas–van Alphen quantum oscillations in a model system, the Bernal-stacked trilayer graphene with dual gates, which shows several highly tunable bands[2–4]. By resolving thermodynamic quantum oscillations spanning more than 100 Landau levels in low magnetic fields, we reconstruct the band structure and its evolution with the displacement field with excellent precision and nanoscale spatial resolution. Moreover, by developing Landau-level interferometry, we show shear-strain-induced pseudomagnetic fields and map their spatial dependence. In contrast to artificially induced large strain, which leads to pseudomagnetic fields of hundreds of tesla[5–7], we detect naturally occurring pseudomagnetic fields as low as 1 mT corresponding to graphene twisting by 1 millidegree, two orders of magnitude lower than the typical angle disorder in twisted bilayer graphene[8–11]. This ability to resolve the local band structure and strain at the nanoscale level enables the characterization and use of tunable band engineering in practical van der Waals devices.

Determining the band structure (BS) and the Fermi surface is a crucial step in understanding and using the electronic properties of materials. The most sensitive canonical method for mapping the BS of bulk metals and semiconductors is the measurement of the de Haas–van Alphen (dHvA) oscillations[12]. In this quantum mechanical effect, in the presence of magnetic field B, electrons coherently circulate in closed electronic orbits, giving rise to quantum oscillations (QOs) in the grand thermodynamic potential Ω and in the associated magnetization $M = -\partial\Omega/\partial B$ (ref. 12). In two-dimensional (2D) systems, these oscillations are described by the formation of Landau energy levels (LLs) with sharp peaks in the density of states (DOS). Charge carriers orbiting in the metallic LL states give rise to diamagnetic response, whereas ground-state currents flowing in the gapped edge states contribute to paramagnetic magnetization, resulting in magnetization oscillations with either magnetic field or carrier density[12]. As the measured total magnetic moment scales with sample volume, observation of dHvA effect in 2D systems has been challenging[13,14], in which non-thermodynamic Shubnikov–de Haas (SdH) oscillations are the benchmark characterization tool[15].

The advances in the fabrication of van der Waals (vdW) atomic layer devices have provided an opportunity for a lot of electronic phases, including tunable correlated insulators[16], orbital magnetism[17–19], integer and fractional Chern insulators[20–23] and unconventional superconductivity[24,25]. Using material selection, stacking order and twist angle, a wide variety of structures with different properties can be engineered. Their BS can be further manipulated through the transverse electric field, magnetic field, strain or pressure. The investigation of the BS in micron-sized vdW devices presently centres on detecting QOs by SdH effect[15,26] and capacitance[4,25]. However, various types of disorder, such as charge inhomogeneity, twist-angle disorder and strain, are seen in these samples[9,27,28], and the aforementioned methods lack spatial information. The various inhomogeneities also obscure the QOs in global measurements, requiring the application of elevated magnetic fields to overcome the spatial disorder. Although several scanning probe techniques, including scanning tunnelling microscopy[29,30] and single-electron transistors[22,31], are powerful probes of local electronic properties, the former requires the electron layers to be exposed to vacuum as in photoemission studies, and neither of them is suitable for devices encapsulated with a metallic top gate required for applying displacement fields. The development of a tool to measure the local BS in the diverse family of 2D quantum materials is thus highly desirable.

Strain emerges as a particularly intriguing, yet challenging, tunable parameter in vdW devices because of their high mechanical flexibility. In addition to changing the BS and breaking of crystal symmetries,

[1]Department of Condensed Matter Physics, Weizmann Institute of Science, Rehovot, Israel. [2]Departments of Physics and Electrical Engineering, University of Colorado Denver, Denver, CO, USA. [3]Research Center for Electronic and Optical Materials, National Institute for Materials Science, Tsukuba, Japan. [4]Research Center for Materials Nanoarchitectonics, National Institute for Materials Science, Tsukuba, Japan. [5]These authors contributed equally: Haibiao Zhou, Nadav Auerbach, Matan Uzan. ✉e-mail: eli.zeldov@weizmann.ac.il

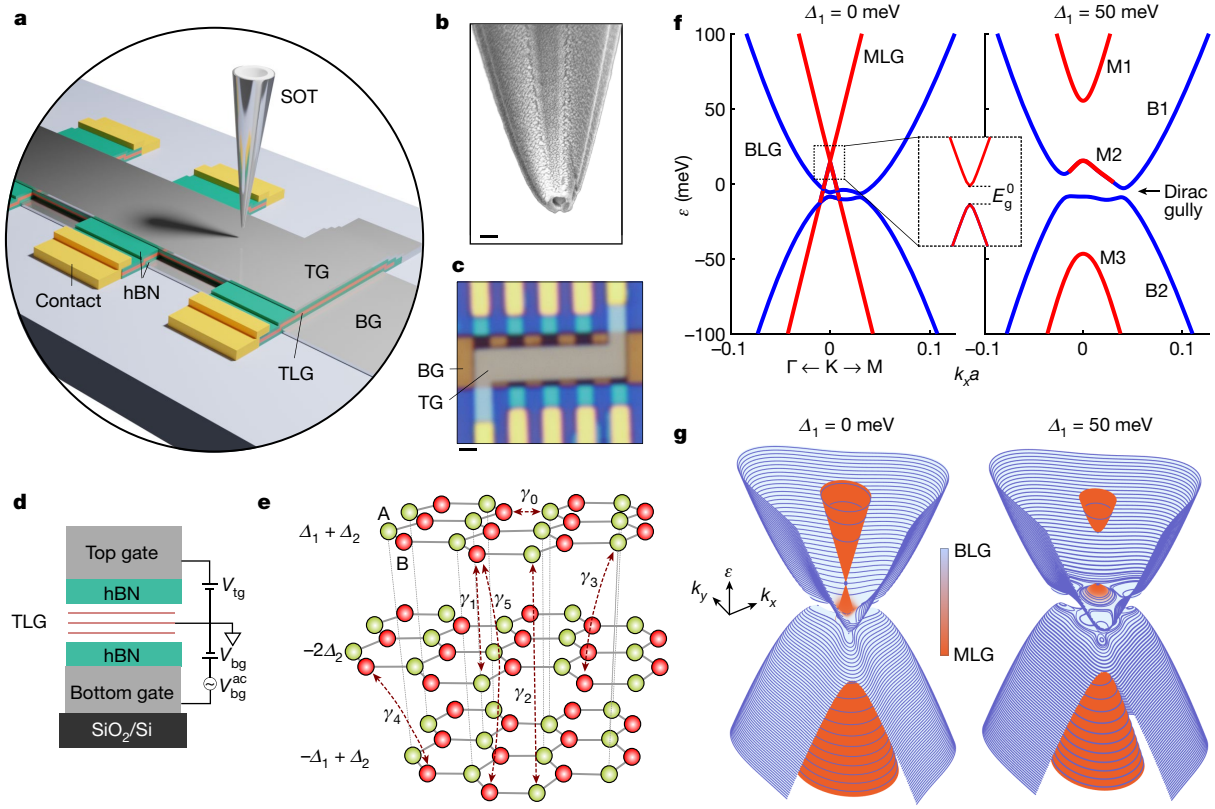

Fig. 1 | Experimental setup and ABA graphene BS. a, Schematic sample structure with TLG encapsulated by hBN and top (TG) and bottom (BG) Pt gates, with scanning SOT. **b**, Scanning electron microscope image of the indium SOT. **c**, Optical image of the TLG device. **d**, The stacking geometry of the device with indicated V_{tg} and V_{bg} voltages applied to the top and bottom gates, respectively, for controlling the carrier density n and displacement field D. **e**, Atomic structure of ABA graphene with indicated SWMc parameters. **f**, The BS of ABA TLG for zero displacement field ($\Delta_1 = 0$ meV) and for $\Delta_1 = 50$ meV. Inset, a small Dirac gap E_g^0 is present in the MLG band at $\Delta_1 = 0$ meV, which grows rapidly with Δ_1. **g**, Three-dimensional rendering of the BS reconstructed from the dHvA oscillations with overlaid contours of the calculated LLs. The LLs are shown for $B_a = 1$ T for clarity. At our $B_a = 320$ mT, the LLs are three times denser. The colour map represents the wavefunction projection onto the MLG-like (red) and BLG-like (blue) bands. Scale bars, 200 nm (**b**) and 1 µm (**c**).

non-uniform strain creates pseudomagnetic fields (PMFs) because of the valley degree of freedom in hexagonal vdW materials[32]. PMFs of tens to hundreds of teslas have been observed in artificially strained graphene nanostructures[6,7]. These gauge fields create effective LLs with sharp peaks in DOS that strongly vary in space and alter the electronic transport properties[5]. Yet, PMFs stemming from the natural strain formed during the fabrication process have remained unknown.

Using scanning SQUID (superconducting quantum interference device)-on-tip (SOT) microscopy[33], we imaged the dHvA effect in hBN-encapsulated dual-gated Bernal-stacked trilayer graphene (TLG) (Fig. 1a). The high magnetic sensitivity of the SOT enables imaging of the QOs at low fields resolving the multi-band electronic structure with sub-meV energy resolution and unperturbed by elevated magnetic fields. The quantitative information provided by the thermodynamic oscillations enables high-precision derivation of the tight-binding hopping parameters and accurate reconstruction of the tunable band hybridization induced by the displacement field. Moreover, the nanoscale spatial resolution enables a detailed quantitative study of the spatial variations of the QOs over the entire device, showing the presence of PMFs of millitesla magnitude in micron-sized domains.

BS of ABA graphene

The Bernal-stacked ABA TLG is the minimal graphene structure requiring the full set of parameters in the Slonczewski–Weiss–McClure (SWMc) tight-binding model[34] (Fig. 1e) with six hopping parameters γ_i ($i = 0$–5), on-site energy difference δ due to stacking, potential difference Δ_1 between the adjacent graphene layers induced by the applied displacement field D and potential difference Δ_2 that describes the non-uniform charge distribution between the middle and the outer layers. The influence of these parameters on the BS is shown in Extended Data Fig. 4.

Owing to the mirror symmetry of the crystal, the bands decompose into a monolayer-graphene (MLG)-like band with Dirac dispersion and a bilayer-graphene (BLG)-like quadratic band, with an energy shift between them (Fig. 1f, left). The D field breaks this symmetry, leading to band hybridization and Lifshitz transitions with multiple changes in the band topology. At high D, the Dirac band divides into three sections (Fig. 1f, right), with M1 and M3 sections separated from the BLG bands B1 and B2, whereas M2 merges with B1 and evolves into gapped mini-Dirac cones at the bottom of B1 (Fig. 1g). These cones (gullies) exhibit three-fold rotational symmetry leading to various possible quantum Hall ferromagnetic and nematic states[35,36].

Previous studies have explored SdH and capacitance oscillations in TLG at elevated fields[3,37,38] to determine the BS and identify broken-symmetry states[4,39,40], yielding a wide span of derived SWMc parameters (Extended Data Table 1), with details of the BS still under debate. In particular, the size and polarity of the Dirac gap, E_g^0, at $D = 0$ (Fig. 1f, inset) is controversial[40]. Moreover, it was predicted that the trigonal warping induced by γ_3 breaks the rotational symmetry with notable consequences on the LL structure, resulting in LL anticrossings, which occur between a given MLG LL and every third BLG LL[36,41]. Although some single anticrossings were reported[40], the predicted periodicity has not been observed directly. Moreover, symmetry breaking leading to gully-polarized states has been reported in high magnetic fields[4], but gully coherence at low fields remains an open question.

Nanoscale magnetic imaging and results

The TLG was encapsulated by approximately 30 nm hBN with top and bottom Pt gates for controlling the carrier density n and displacement field D (Fig. 1 and Methods). Transport measurements of R_{xx} versus n and applied magnetic field B_a show a Landau fan with several LL crossings (Extended Data Fig. 1), similar to those in previous reports[40]. Local dHvA oscillations measurements were performed using indium SOT of 150 nm diameter at a height of $h \approx 150$ nm above the graphene at $T \approx 160$ mK (Fig. 1b and Methods). A small a.c. voltage V_{bg}^{ac} at about 1.8 kHz modulates n by n^{ac}, inducing a local a.c. magnetic field B_z^{ac} recorded by the scanning SOT. This B_z^{ac} reflects the differential change m_z in the local orbital magnetization M_z, $m_z = \partial M_z/\partial n$.

Figure 2c shows dHvA oscillations acquired at $B_a = 320$ mT at a single point above the sample versus D and low carrier densities n between -1.2×10^{12} cm^{-2} and 2.3×10^{12} cm^{-2}. A line cut of the data at $D = 0$ V nm^{-1} is shown in Fig. 2a. Notably, in this relatively small n range, we observe more than 100 LLs, in sharp contrast to transport measurements (Extended Data Fig. 1), in which no SdH oscillations can be discerned at such low B_a. Moreover, we can resolve dHvA oscillations at fields as low as 40 mT (Extended Data Fig. 2). To our knowledge, this is the lowest B_a at which QOs have been observed in 2D systems. As shown in Fig. 1g, mapping these dense LLs offers a distinctive quantitative approach for high-precision BS reconstruction and derivation of high-accuracy SWMc parameters as summarized in Extended Data Table 1.

Figure 2b,d shows dHvA oscillations calculated from the fitted BS, showing remarkable qualitative and quantitative agreement with the experiment. Such accurate reconstruction is possible because the thermodynamic QOs can be calculated quantitatively from the BS (Methods). The observed QOs can be classified by five sets of LLs.

In the B1 and B2 bands, as the DOS in the BLG bands is much higher than in MLG bands, the LLs in B1 and B2 bands appear as dense horizontal lines in Fig. 2c,d. At low fields, the LLs are four-fold valley and spin degenerate, dispersing as approximately $\pm\sqrt{n_B(n_B-1)}\,B_a$ where n_B is the BLG LL index. At $B_a = 320$ mT, the energy spacing between the B1 LLs is about 1 meV and 0.6 meV in B2, defining our energy resolution of better than 0.6 meV.

In the M1 band, the MLG LLs disperse as approximately $\pm\sqrt{|n_M|\,B_a}$ and are much sparser because of the low DOS. Displacement field opens a large gap E_g between the MLG sections (Fig. 1f,g) resulting in parabolic-like upturn of M1 LLs with D in Fig. 2c,d. At LL crossings, B1 LLs show a phase shift because an M1 LL has to be filled before subsequent B1 LLs can be occupied, with the shift magnitude determined by the LL degeneracy. The high M1 LLs are four-fold degenerate, causing a 2π phase shift as indicated by the dotted white line in Fig. 2c,e. Owing to the topological nature of the Dirac point, the zeroth MLG LLs are valley polarized with 0_{M1}^- LL (zeroth LL in K$^-$ valley) residing at the bottom of the M1 band, whereas 0_{M2}^+ LL (zeroth LL in K$^+$ valley) is pinned to the top of the M2 band. As these two zeroth LLs are two-fold spin degenerate[36,41], their crossing with the four-fold degenerate B1 LLs results in a π rather than a 2π shift (Fig. 2c,e, red dotted lines). Moreover, higher M1 LLs show a pronounced negative (dark) diamagnetic signal[42]. By contrast, the 0_{M1}^- and 0_{M2}^+ LLs in Fig. 2c–e are invisible with their presence discerned by only B1 LLs phase shift. This arises from the Berry phase pinning of the zeroth LL compressible states to band extrema with zero kinetic energy and hence no diamagnetism. However, the incompressible states in the MLG LL gaps show a paramagnetic response[42] determined by the Chern number C as shown in Extended Data Fig. 2e.

In the M2 band, the band hybridization results in a small M2 hole pocket with the total DOS that is too low to accommodate even a single LL at elevated B_a. Consequently, the M2 LLs could not be identified previously[4,37,40]. Our low B_a and high sensitivity enable clear resolution of M2 LLs (Fig. 2c–e and Extended Data Fig. 2). Figure 2e also shows a gap E_g^0 between the 0_{M1}^- and 0_{M2}^+ LLs at $D = 0$, comparable to the gap between the two B1 LLs (about 1 meV). The zeroth LLs rapidly separate with D, indicating that E_g grows continuously without intermediate gap closure, contrary to previous suggestions[4,40].

In the M3 band, at elevated hole doping, the M3 LLs mirror the behaviour of M1 LLs. At low doping, in contrast, the strong hybridization between M3 and B2 bands induces unusual valley polarization. This is demonstrated in Fig. 2f, in which the four-fold degenerate -1_{M3} LL splits into valley polarized -1_{M3}^+ and -1_{M3}^- LLs, accompanied by multiple LL crossings and anticrossings (Extended Data Fig. 6). In particular, avoided crossings with every third BLG LL have been predicted[36,41] because of trigonal warping. This triple period, unidentified so far, to our knowledge, is resolved in our data (white bars in Fig. 2f) in agreement with the calculations in Extended Data Fig. 6. We also resolve the 0_{M3}^- LL with no diamagnetism, which induces a π shift in the B2 LLs (Fig. 2f, red dotted line).

In LLs in the gullies, near charge neutrality point (CNP), on increasing D, the enhanced band hybridization and trigonal warping results in three-fold rotationally symmetric Dirac gullies[36,41] with highly intriguing LL evolution. The low-energy BLG LLs, which are mostly valley degenerate at $D = 0$, undergo valley polarization and intertwining, forming valley-polarized six-fold degenerate LLs in the gully pockets (Extended Data Fig. 3f). The zeroth gully LLs, 0_G^- and 0_G^+, exhibit no diamagnetism and the Δ_G^0 gap between them has $C = 0$. Consequently, a magnetism-free strip of width corresponding to 12-fold degeneracy (0_G^-, 0_G^+ and Δ_G^0) is observed around the CNP in Fig. 2c,d,f at elevated D. The positive and negative (yellow and blue) signals outside the strip are the paramagnetic responses in the LL gaps Δ_G^1 and Δ_G^{-1} (Fig. 2f and Extended Data Fig. 3e,f).

The marked consistency between the experimental data (Fig. 2c) and the single-particle BS calculations (Fig. 2d) across the entire (n, D) plane suggests that the electron–electron interactions play a negligible part in ABA graphene at low B_a and that the band parameters do not vary in our accessible parameter range. Our dHvA imaging technique is also applicable to moiré systems as demonstrated in Extended Data Fig. 9 for twisted double bilayer graphene, showcasing intricate crossings between LLs in flat and dispersive bands, which can provide indispensable information for the study of correlation effects.

LL interferometry and strain-induced PMF

Next, we analyse QOs over the full range of accessible carrier densities $|n| \lesssim 9 \times 10^{12}$ cm^{-2}, which enables resolving much finer details of the BS and its spatial dependence. Because at $B_a = 320$ mT in this n range there are about 500 BLG and more than 100 MLG LLs, we focus on the sparser MLG LLs by applying a larger V_{bg}^{ac} (Methods). Figure 3a–d shows the spatial dependence of $B_z^{ac}(x, y)$ at several densities, whereas Fig. 3f presents $B_z^{ac}(x)$ versus n along the dotted line in Fig. 3a. For $|n| \lesssim 3 \times 10^{12}$ cm^{-2}, shown in Fig. 2, the QOs exhibit relatively high spatial uniformity as shown in Fig. 3d and at the bottom of Fig. 3f, demonstrating high sample quality. At higher n, however, distinctly different behaviour is observed depending on the location as demonstrated in Fig. 3g,h showing the QOs at sites A and B indicated in Fig. 3b. Large parts of the sample, exemplified by site A, show continuous evolution of QOs (Fig. 3g), consistent with the calculations. In other parts of the sample as site B, however, striking low-frequency beating of the MLG LLs is found (Fig. 3h). At a lower $B_a = 170$ mT, the beating nodes are shifted to lower LL indices (Fig. 3i).

As the MLG and BLG bands have very different dispersions, the beating cannot arise from their interference. It must therefore originate from small symmetry breaking between the four flavours of the MLG band. In the Methods, we consider various possible mechanisms, including staggered substrate potential, Kekulé distortions, band shifting, Zeeman effects and spin–orbit coupling, as well as non-symmetry-breaking disorder, and show that they are inconsistent with the observed behaviour. Below, we demonstrate that the interference of the QOs is well described by strain-induced PMF (B_S).

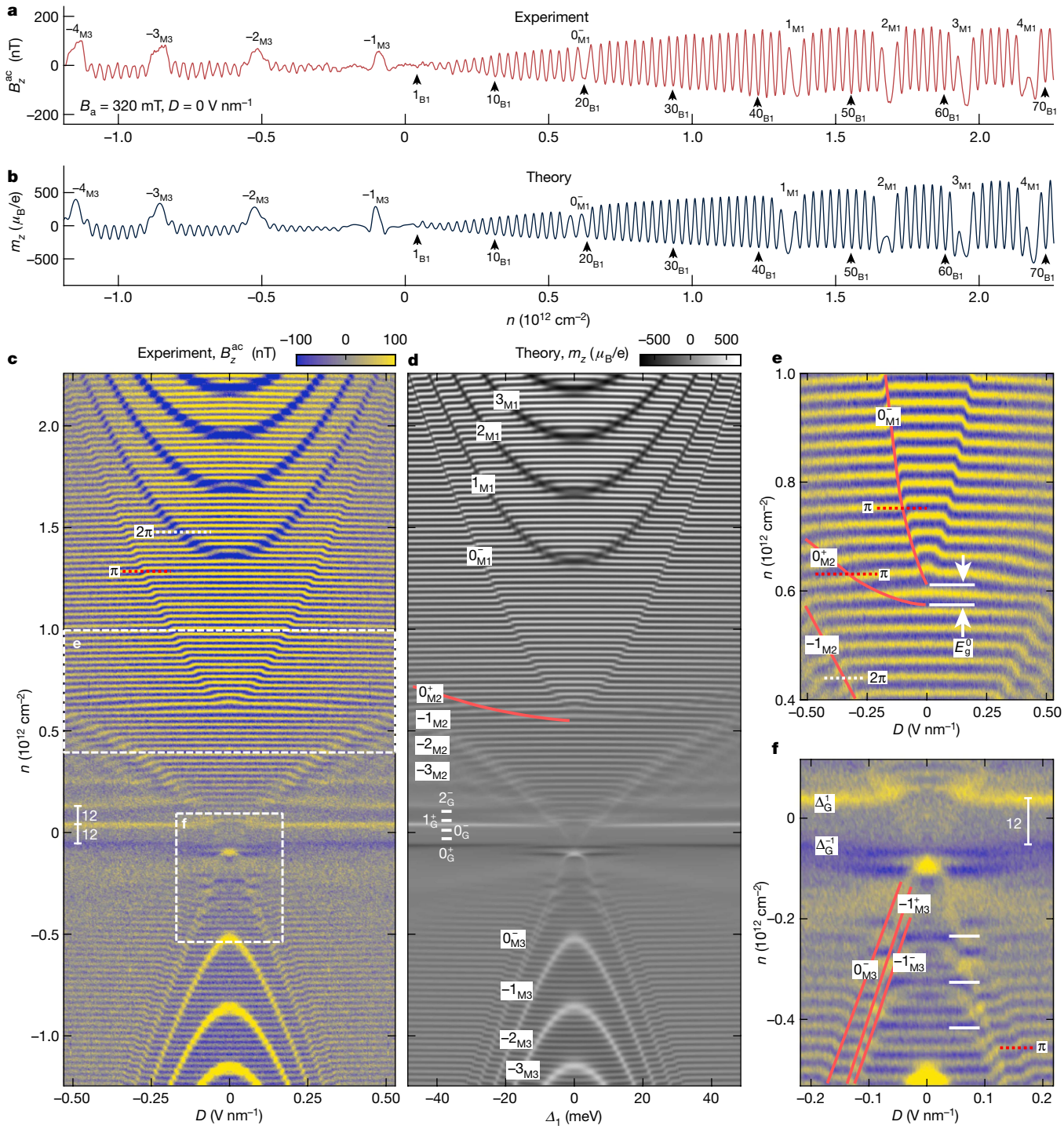

Fig. 2 | Measurement of dHvA effect in ABA graphene. a, The measured local magnetic QOs signal B_z^{ac} as a function of n at 160 mK at a fixed location in the interior of the sample at B_a = 320 mT and D = 0 V nm^{-1} using V_{bg}^{ac} = 8 mV rms. Some indices of the LLs in M1, B1 and M3 bands are indicated. **b**, The calculated dHvA differential magnetization m_z at D = 0 V nm^{-1} using the derived BS. **c**, The measured B_z^{ac} versus n and D. Crossings between the four-fold degenerate BLG LLs (horizontal yellow and blue lines) and the zeroth K$^-$ valley MLG LL, 0_{M1}^-, results in a π shift (red dotted line), whereas crossing with the higher MLG LLs introduces a 2π shift (white dotted line). The white vertical bars indicate the 12-fold degeneracy of the LLs in the gullies. **d**, Calculated $m_z(n, D)$ using the fitted SWMc tight-binding parameters with Dingle broadening of 0.3 meV. The MLG LLs in M1, M2 and M3 bands and the gully LLs are labelled. **e**, Magnification of the measured $B_z^{ac}(n, D)$ in the vicinity of MLG Dirac gap E_g (dashed rectangle in **c**) with marked MLG LLs (red). The π shifts at crossings between BLG and 0_{M2}^+ and 0_{M1}^- valley-polarized MLG LLs and 2π shift at crossing of valley degenerate -1_{M2} LL are indicated. **f**, Magnification of $B_z^{ac}(n, D)$ near the top of the BLG valence band B2 showing anticrossings between the MLG and BLG LLs. The white horizontal bars indicate enlarged anticrossing gaps for every third BLG LL (Extended Data Fig. 6).

Long-wavelength mechanical strain induces an effective gauge field in graphene, with opposite signs for the two valleys. Isotropic or uniaxial strains yield zero PMF, whereas non-uniform shear strain produces a finite B_S (ref. 32). In the presence of B_a, carriers in the K$^+$ and K$^-$ valleys experience effective fields B_{eff} of $B_a + B_S$ and $B_a - B_S$, inducing a relative shift in the LLs and interference (Fig. 4a). In the MLG Dirac band, the LL energies are given by $E_N = \sqrt{2e\hbar v_F^2 B_{eff} N}$, where e is the elementary charge, $\hbar$ is the reduced Plank constant and v_F is the Fermi velocity.

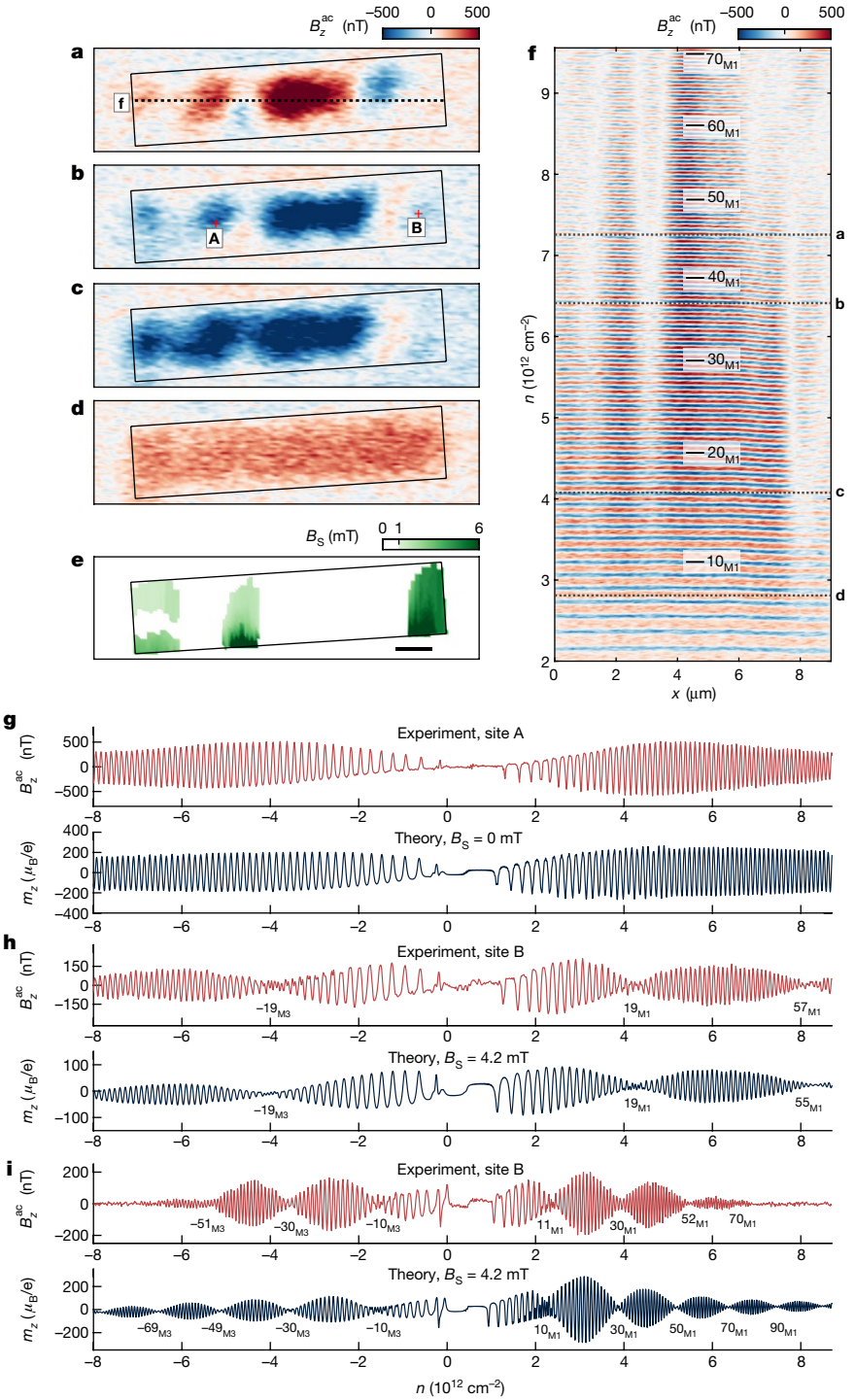

Fig. 3 | Imaging the beating of QOs and mapping the PMFs. a–**d**, Spatial imaging of $B_z^{ac}(x, y)$ at B_a = 320 mT and $n = 7.26 \times 10^{12}$ cm^{-2} (**a**), 6.41×10^{12} cm^{-2} (**b**), 4.08×10^{12} cm^{-2} (**c**) and 2.81×10^{12} cm^{-2} (**d**) corresponding to dotted lines in **f**. The black rectangle indicates the boundaries of the TLG. **e**, Map of the derived PMF B_S across the sample. Regions with B_S below our resolution of 1 mT are shaded in white. **f**, Line scans of $B_z^{ac}(x)$ versus n measured along the dotted line marked in **a** showing QOs from the MLG LLs in the M1 band. **g**, The measured QOs due to MLG LLs (top) at location A indicated in **b** and the calculated QOs (bottom). **h**, The measured QOs (top) at location B and the calculated QOs (bottom) with B_S = 4.2 mT. The LL indices at the beating nodes are indicated. **i**, Same as **h** at B_a = 170 mT. The applied larger V_{bg}^{ac} = 10 mV rms in **a**–**d** and **i**, and 20 mV rms in **f**–**h** averages out the QOs due to BLG LLs intensifying the visibility of MLG LLs. Scale bar, 1 μm (**e**).

Hence for $B_S \ll B_a$, the energy shift between the LLs in the two valleys is $\delta E_N = \sqrt{2e\hbar v_F^2 N}\,(\sqrt{B_a + B_S} - \sqrt{B_a - B_S}) \approx B_S\sqrt{2e\hbar v_F^2 N/B_a}$. Because δE_N scales with $\sqrt{N}$, the lowest LLs remain almost degenerate. For higher LLs, the relative shift between the valley-polarized LLs grows continuously with energy, resulting in beating. The first destructive interference occurs when $\delta E_N = \Delta E_N/2$, where $\Delta E_N = E_{N+1} - E_N \approx \sqrt{e\hbar v_F^2 B_a/2N}$ is the LL energy spacing, resulting in the first beating node at $N = N_b^1 = B_a/4B_S$.

Figure 4b shows the theoretical N_b^1 dependence on B_S, and the calculated beating patterns of the QOs versus B_S are presented in Fig. 4d. At the nodes, the K^+ and K^- LLs are out of phase, resulting in amplitude suppression and a barely visible frequency doubling. In Fig. 3h

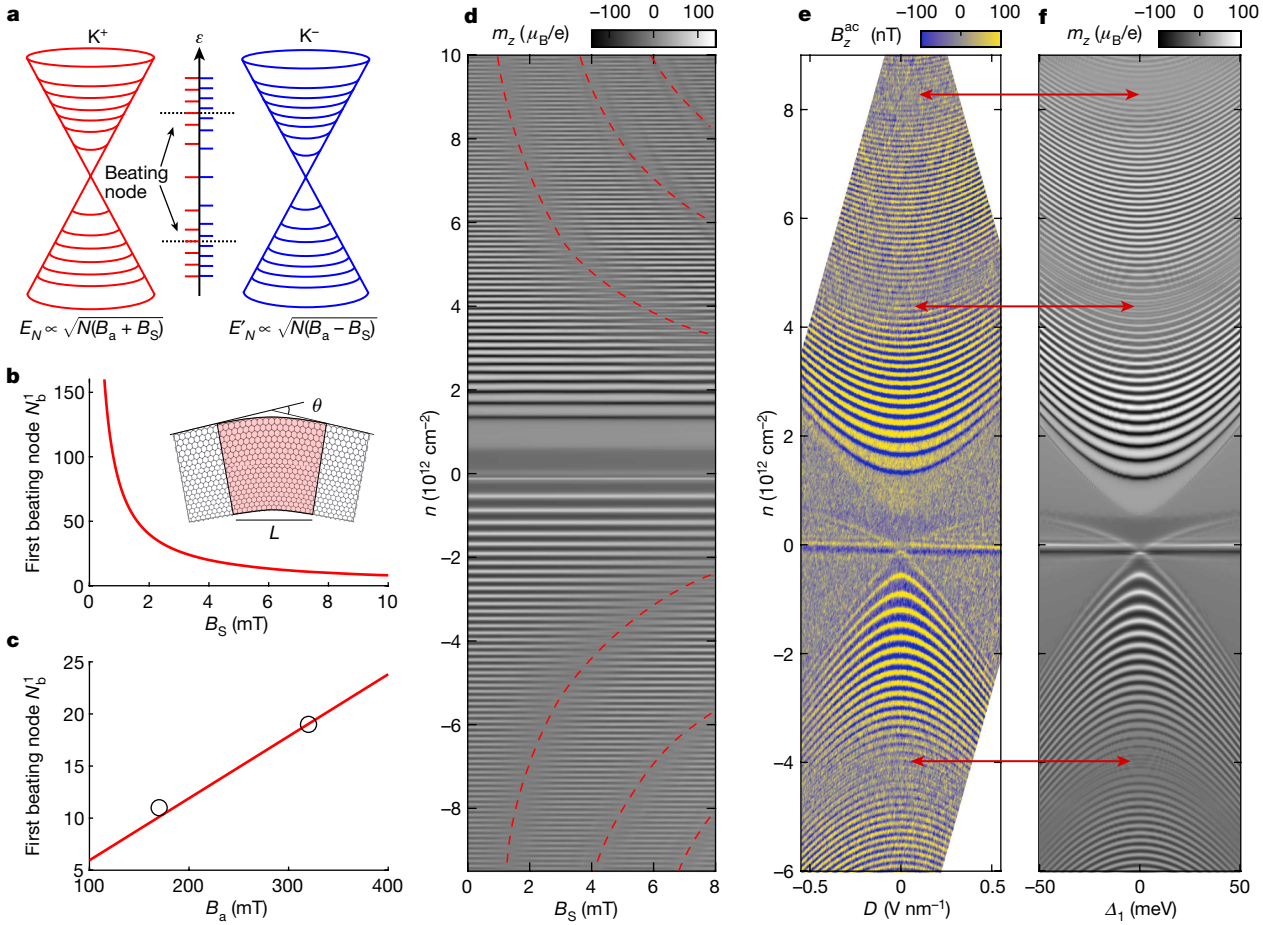

Fig. 4 | LL interferometry of strain-induced PMF. a, Schematic of LL beating in the presence of PMF (B_S) in graphene. Only the MLG Dirac bands with LLs are shown for clarity. **b**, The LL index of the first beating node N_b^1 in the Dirac band versus B_S at $B_a = 320$ mT. Inset, schematic of a graphene strip with arc-like bent section (red) of length L and bend angle θ generating strain-induced B_S. The illustrated θ is greatly exaggerated compared with the maximal derived $\theta \approx 6 \times 10^{-3}$ degrees. **c**, Calculated dependence of N_b^1 on B_a for $B_S = 4.2$ mT (red). The open circles show the measured N_b^1 at $B_a = 170$ mT and 320 mT. **d**, Calculated QOs in the MLG band versus n and B_S at $B_a = 320$ mT and $D = 0$ V nm^{-1}. The locations of the beating nodes N_b^1 to N_b^3 are highlighted in red. **e**, The measured QOs in the MLG bands versus n and D using $V_{bg}^{ac} = 20$ mV rms showing beating nodes (red arrows). **f**, Calculated QOs versus n and D at $B_a = 320$ mT and $B_S = 4.2$ mT.

(red curve), we observe the first node at $N_b^1 = 19$, yielding $B_S = B_a/4N_b^1 = 4.2$ mT. The calculated QOs with $B_S = 4.2$ mT (black curve) show an excellent agreement with the data and also well reproduce the secondary nodes at −19 and 57. Moreover, the observed evolution of the interference with D (Fig. 4e) is well reproduced by the simulations (Fig. 4f), both in the position of all the three beating nodes (red arrows) and in their evolution with D using a single fitting parameter B_S. Because the BS changes profoundly with D and the strain-induced PMF should be independent of the BS, the fact that the observed beating is well described by a D-independent B_S provides extra strong support for the model. Furthermore, the PMF should affect all the bands. An important self-consistency check is, therefore, the observation of beating also in the BLG LLs.

Extended Data Fig. 7 shows a closer examination of the BLG QOs at the same location B. Beating is observed and well reproduced by simulations using the same set of parameters. Finally, a crucial test of the PMF origin of the interference is the predicted linear dependence of N_b^1 on B_a, distinguishing it from other possible mechanisms (Methods). Figure 3i (red curve) presents the LL interference measured at $B_a = 170$ mT, showing several beating nodes. The calculated QOs (black curve) show an excellent agreement with the data, confirming the linear dependence (Fig. 4c).

Analysing the LL interference over the entire sample, we derive a map of B_S (Fig. 3e). In large regions, B_S is below our resolution of about 1 mT, set by the highest accessible n (Methods). We find four regions with characteristic length $L \approx 1$ μm with smoothly varying B_S reaching up to 6 mT. Several types of lattice distortion—finely tuned triaxial strain, arc-like in-plane bending or stretching a trapezoid-like geometry—have been shown theoretically to produce relatively homogenous B_S (refs. 5,43,44). In our sample, the strain probably arises because of the in-plane bending introduced during the fabrication processes (Fig. 4b, inset). An arc segment of length L with a twist angle θ in a graphene strip generates $B_S \approx c\beta\frac{\phi_0}{aL}\theta$ (ref. 43), where $a = 0.14$ nm is the graphene interatomic distance, $c \approx 1$ is a numerical constant, $\beta \approx 2$ describes the hopping parameter dependence on a, $\phi_0 = h/e$ is the flux quantum and h is the Planck constant. The measured $1 < B_S < 6$ mT thus corresponds to twisting by $1 < \theta < 6$ millidegrees, or equivalently bending radius of $1 < R < 6$ cm and corresponding strain of $8 \times 10^{-6} < \bar{u} < 5 \times 10^{-5}$, where $R = L/\theta$ and $\bar{u} = \theta/2$ (ref. 43). These minute bending angles and strains should be abundant in exfoliated atomic layer devices. Strains of larger orders of magnitude and angle disorder have been reported to occur naturally in twisted and stacked graphene structures[8–11,30,45].

Discussion

The local dHvA QO technique developed provides a tool for high-precision, quantitative reconstruction of the BS in 2D materials and of its spatial dependence at the nanoscale level. Unlike global

measurements, which are affected by spatial inhomogeneities and strain, the local dHvA effect offers high energy resolution approaching the limit of intrinsic lifetime broadening of the energy bands. Moreover, the magnetic QOs are not obscured by metallic gates and multilayer structures, enabling investigation of most of the state-of-the-art vdW devices with in situ tunable BS. Most importantly, the method is not limited to single-particle physics and can show the BS governed by many-body effects and strong interactions in flat-band materials. It can thus improve our modelling and understanding of a wide range of strongly correlated 2D systems and moiré quantum materials.

The strain-induced PMFs have important implications for our comprehension of disorder and their impact on strongly correlated states. In particular, twisted bilayer and multilayer graphene are known to be susceptible to twist-angle disorder. Spatial variations in twist angle and strain induce fluctuations in the bandwidth of the flat bands, electron interactions and the emergence of symmetry-broken states[46]. Yet, the effects of the accompanying spatially varying PMFs have not been investigated experimentally. Our findings indicate that the typical reported twist-angle disorder of 0.1° (refs. 8–11) can generate $B_S \approx 0.1$ T, markedly influencing magnetotransport behaviour. Resolving LLs in transport at low fields is challenging in twisted devices, potentially arising from such highly spatially varying PMFs. Moreover, in the presence of a magnetic field, the PMF breaks the valley symmetry resulting in different DOS in the two valleys. B_S fluctuations may thus affect the local Stoner instabilities and symmetry-breaking mechanisms that lead to the quantum anomalous Hall effect, Chern insulators and inhomogeneities in the spontaneous orbital magnetization[18–20]. Finally, the recent development of programmable in-plane bending of graphene ribbons[47] provides an opportunity for microscale engineering and exploitation of PMFs towards the realization of zero-field quantum Hall and topological insulator-like states[5] and of all-graphene electronics[48]. The derived method of high-precision determination of local BS and PMF imaging provides a powerful tool for the characterization and optimization of tunable electronic bands and calls for further investigation of the role of strain-induced gauge fields in the formation of symmetry-broken, strongly correlated states of matter.

Online content

Any methods, additional references, Nature Portfolio reporting summaries, source data, extended data, supplementary information, acknowledgements, peer review information; details of author contributions and competing interests; and statements of data and code availability are available at https://doi.org/10.1038/s41586-023-06763-5.

1. Andrei, E. Y. et al. The marvels of moiré materials. *Nat. Rev. Mater.* **6**, 201–206 (2021).
2. Koshino, M. & McCann, E. Gate-induced interlayer asymmetry in ABA-stacked trilayer graphene. *Phys. Rev. B* **79**, 125443 (2009).
3. Taychatanapat, T., Watanabe, K., Taniguchi, T. & Jarillo-Herrero, P. Quantum Hall effect and Landau-level crossing of Dirac fermions in trilayer graphene. *Nat. Phys.* **7**, 621–625 (2011).
4. Zibrov, A. A. et al. Emergent Dirac gullies and gully-symmetry-breaking quantum Hall states in *ABA* trilayer graphene. *Phys. Rev. Lett.* **121**, 167601 (2018).
5. Guinea, F., Katsnelson, M. I. & Geim, A. K. Energy gaps and a zero-field quantum Hall effect in graphene by strain engineering. *Nat. Phys.* **6**, 30–33 (2010).
6. Levy, N. et al. Strain-induced pseudo–magnetic fields greater than 300 tesla in graphene nanobubbles. *Science* **329**, 544–547 (2010).
7. Mao, J. et al. Evidence of flat bands and correlated states in buckled graphene superlattices. *Nature* **584**, 215–220 (2020).
8. Yoo, H. et al. Atomic and electronic reconstruction at the van der Waals interface in twisted bilayer graphene. *Nat. Mater.* **18**, 448–453 (2019).
9. Uri, A. et al. Mapping the twist-angle disorder and Landau levels in magic-angle graphene. *Nature* **581**, 47–52 (2020).
10. Kazmierczak, N. P. et al. Strain fields in twisted bilayer graphene. *Nat. Mater.* **20**, 956–963 (2021).
11. Halbertal, D., Shabani, S., Passupathy, A. N. & Basov, D. N. Extracting the strain matrix and twist angle from the moiré superlattice in van der Waals heterostructures. *ACS Nano* **16**, 1471–1476 (2022).
12. Shoenberg, D. *Magnetic Oscillations in Metals* (Cambridge Univ. Press, 1984).
13. Wilde, M. A. et al. Experimental evidence of the ideal de Haas-van Alphen effect in a two-dimensional system. *Phys. Rev. B* **73**, 125325 (2006).
14. Vallejo Bustamante, J. et al. Detection of graphene's divergent orbital diamagnetism at the Dirac point. *Science* **374**, 1399–1402 (2021).
15. Novoselov, K. S. et al. Two-dimensional gas of massless Dirac fermions in graphene. *Nature* **438**, 197–200 (2005).
16. Cao, Y. et al. Correlated insulator behaviour at half-filling in magic-angle graphene superlattices. *Nature* **556**, 80–84 (2018).
17. Sharpe, A. L. et al. Emergent ferromagnetism near three-quarters filling in twisted bilayer graphene. *Science* **365**, 605–608 (2019).
18. Tschirhart, C. L. et al. Imaging orbital ferromagnetism in a moiré Chern insulator. *Science* **372**, 1323–1327 (2021).
19. Grover, S. et al. Chern mosaic and Berry-curvature magnetism in magic-angle graphene. *Nat. Phys.* **18**, 885–892 (2022).
20. Lu, X. et al. Superconductors, orbital magnets and correlated states in magic-angle bilayer graphene. *Nature* **574**, 653–657 (2019).
21. Li, T. et al. Quantum anomalous Hall effect from intertwined moiré bands. *Nature* **600**, 641–646 (2021).
22. Xie, Y. et al. Fractional Chern insulators in magic-angle twisted bilayer graphene. *Nature* **600**, 439–443 (2021).
23. Cai, J. et al. Signatures of fractional quantum anomalous Hall states in twisted $MoTe_2$. *Nature* **622**, 63–68 (2023).
24. Cao, Y. et al. Unconventional superconductivity in magic-angle graphene superlattices. *Nature* **556**, 43–50 (2018).
25. Zhou, H. et al. Isospin magnetism and spin-polarized superconductivity in Bernal bilayer graphene. *Science* **375**, 774–778 (2022).
26. Zhang, Y., Tan, Y.-W., Stormer, H. L. & Kim, P. Experimental observation of the quantum Hall effect and Berry's phase in graphene. *Nature* **438**, 201–204 (2005).
27. Martin, J. et al. Observation of electron–hole puddles in graphene using a scanning single-electron transistor. *Nat. Phys.* **4**, 144–148 (2008).
28. Halbertal, D. et al. Unconventional non-local relaxation dynamics in a twisted trilayer graphene moiré superlattice. *Nat. Commun.* **13**, 7587 (2022).
29. Xie, Y. et al. Spectroscopic signatures of many-body correlations in magic-angle twisted bilayer graphene. *Nature* **572**, 101–105 (2019).
30. Choi, Y. et al. Correlation-driven topological phases in magic-angle twisted bilayer graphene. *Nature* **589**, 536–541 (2021).
31. Zondiner, U. et al. Cascade of phase transitions and Dirac revivals in magic-angle graphene. *Nature* **582**, 203–208 (2020).
32. Vozmediano, M. A. H., Katsnelson, M. I. & Guinea, F. Gauge fields in graphene. *Phys. Rep.* **496**, 109–148 (2010).
33. Vasyukov, D. et al. A scanning superconducting quantum interference device with single electron spin sensitivity. *Nat. Nanotechnol.* **8**, 639–644 (2013).
34. Dresselhaus, M. S. & Dresselhaus, G. Intercalation compounds of graphite. *Adv. Phys.* **51**, 1–186 (2002).
35. Morimoto, T. & Koshino, M. Gate-induced Dirac cones in multilayer graphenes. *Phys. Rev. B* **87**, 085424 (2013).
36. Serbyn, M. & Abanin, D. A. New Dirac points and multiple Landau level crossings in biased trilayer graphene. *Phys. Rev. B* **87**, 115422 (2013).
37. Campos, L. C. et al. Landau level splittings, phase transitions, and nonuniform charge distribution in trilayer graphene. *Phys. Rev. Lett.* **117**, 066601 (2016).
38. Che, S. et al. Substrate-dependent band structures in trilayer graphene/h-BN heterostructures. *Phys. Rev. Lett.* **125**, 246401 (2020).
39. Lee, Y. et al. Broken symmetry quantum Hall states in dual-gated ABA trilayer graphene. *Nano Lett.* **13**, 1627–1631 (2013).
40. Datta, B. et al. Landau level diagram and the continuous rotational symmetry breaking in trilayer graphene. *Phys. Rev. Lett.* **121**, 056801 (2018).
41. Koshino, M. & McCann, E. Landau level spectra and the quantum Hall effect of multilayer graphene. *Phys. Rev. B* **83**, 165443 (2011).
42. Uri, A. et al. Nanoscale imaging of equilibrium quantum Hall edge currents and of the magnetic monopole response in graphene. *Nat. Phys.* **16**, 164–170 (2019).
43. Guinea, F., Geim, A. K., Katsnelson, M. I. & Novoselov, K. S. Generating quantizing pseudomagnetic fields by bending graphene ribbons. *Phys. Rev. B* **81**, 035408 (2010).
44. Zhu, S., Stroscio, J. A. & Li, T. Programmable extreme pseudomagnetic fields in graphene by a uniaxial stretch. *Phys. Rev. Lett.* **115**, 245501 (2015).
45. Turkel, S. et al. Orderly disorder in magic-angle twisted trilayer graphene. *Science* **376**, 193–199 (2022).
46. Nuckolls, K. P. et al. Quantum textures of the many-body wavefunctions in magic-angle graphene. *Nature* **620**, 525–532 (2023).
47. Kapfer, M. et al. Programming twist angle and strain profiles in 2D materials. *Science* **381**, 677–681 (2023).
48. Pereira, V. M. & Castro Neto, A. H. Strain engineering of graphene's electronic structure. *Phys. Rev. Lett.* **103**, 046801 (2009).

Methods

Device fabrication

The hBN-encapsulated ABA graphene heterostructure was fabricated using the dry-transfer method. The graphene flakes were first exfoliated onto a Si/SiO_2 (285 nm) substrate. The number of layers in the graphene flakes was determined using Raman microscopy[49]. Then, the hBN (about 30 nm thick) and the graphene flakes were picked up using a polycarbonate on a polydimethylsiloxane dome stamp. The stacks were then released onto a pre-annealed Ti (2 nm)/Pt (10 nm) bottom gate, patterned on the Si/SiO_2 wafer. The finalized stacks were annealed in a vacuum at 500 °C for strain release[50]. A Ti (2 nm)/Pt (10 nm) top gate was then deposited on top of the stack. The one-dimensional contacts were formed by SF_6 and O_2 plasma etching followed by evaporating Cr (4 nm)/Au (70 nm). Then, the device was etched into a Hall bar geometry. Finally, the device was re-annealed at 350 °C in a vacuum. The capacitances per unit area of the bottom and top gates are $C_{bg} = 0.649 \times 10^{12}\, e\ cm^{-2}\ V^{-1}$, $C_{tg} = 0.668 \times 10^{12}\, e\ cm^{-2}\ V^{-1}$. The top and bottom gates are used to control the carrier density $n = (C_{bg}V_{bg} + C_{tg}V_{tg})/e$ and the effective transverse displacement field $D = (C_{tg}V_{tg} - C_{bg}V_{bg})/2\varepsilon_0$, where ε_0 is vacuum permittivity. From fitting the experimental QOs to simulations, we find that $D = 1\ V\ nm^{-1}$ corresponds to the energy difference between the adjacent graphene layers of $\Delta_1 = 92$ meV.

Transport measurements

Transport characterization of ABA graphene devices was carried out using standard lock-in techniques. The R_{xx} shows a peak along the diagonal charge neutrality line that increases with D, suggesting a gap opening (Extended Data Fig. 1a). The Landau fan shows LL crossings (Extended Data Fig. 1b), consistent with the previous reports[3,37,38,40,51–56]. The QOs from MLG band LLs are visible at low fields, but the BLG LLs can be only resolved above 0.75 T on the electron side and at notably higher fields on the hole doping side (Extended Data Fig. 1c).

SOT measurements and magnetization reconstruction

The local magnetic measurements were conducted in a custom-built scanning SOT microscope in a cryogen-free dilution refrigerator (Leiden CF1200) at a temperature of 160–350 mK (ref. 57). Indium SOT with an effective diameter of about 150 nm and magnetic sensitivity of 20 nT $Hz^{-1/2}$ was fabricated as described previously[33,58,59]. The SOT readout circuit is based on SQUID series array amplifier[60,61]. The SOT is attached to a quartz tuning fork vibrating at about 32.8 kHz (Model TB38, HMI Frequency Technology), which is used as a force sensor for tip height control[62]. The scanning height was about 150 nm above the ABA graphene. An a.c. voltage V_{bg}^{ac} at a frequency of about 1.8 kHz was applied to the bottom gate to modulate the carrier density by $n^{ac} = C_{bg}V_{bg}^{ac}/e$. A lock-in amplifier was used to measure the corresponding local B_z^{ac} by the scanning SOT. The B_z^{ac} data were symmetrized with respect to the displacement field D where applicable. In contrast to other scanning techniques, the magnetic signal is transparent to the metallic top gate, enabling the investigation of a wide range of heterostructures and encapsulated devices.

The 2D $B_z^{ac}(x, y)$ images were used to reconstruct the magnetization $m_z(x, y)$ using the numerical inversion procedure described in ref. 63 (Extended Data Fig. 2). As the reconstruction of m_z requires 2D $B_z^{ac}(x, y)$ information, the QOs at a single location or along the one-dimensional line scans are presented in the main text as the raw data of B_z^{ac}.

Magnetic field and modulation amplitude dependence of QOs

The measured signal $B_z^{ac} = n^{ac}(dB_z/dn)$ is proportional to the modulation amplitude of the carrier density n^{ac} induced by V_{bg}^{ac}. It is therefore desirable to use large n^{ac} to improve the signal-to-noise ratio. To resolve QOs, however, n^{ac} has to be substantially smaller than the period of the oscillations Δn. Extended Data Fig. 2c–e shows the QOs acquired at $B_a = 320$ mT using $V_{bg}^{ac} = 8$ mV, 35 mV and 100 mV rms corresponding to n^{ac} of $5.19 \times 10^9\ cm^{-2}$, $2.27 \times 10^{10}\ cm^{-2}$ and $6.49 \times 10^{11}\ cm^{-2}$ rms, respectively. The four-fold degenerate BLG LLs have a period of $\Delta n = 4B_a/\phi_0 = 3.1 \times 10^{10}\ cm^{-2}$. The lowest $V_{bg}^{ac} = 8$ mV rms was chosen to result in a peak-to-peak value of n^{ac} of $1.47 \times 10^{10}\ cm^{-2}$, approximately equal to $\Delta n/2 = 1.55 \times 10^{10}\ cm^{-2}$, which results in an optimal signal-to-noise ratio for detecting the BLG LLs, albeit suppresses the measured B_z^{ac}/n^{ac} ratio by a factor of π/2. A larger n^{ac} washes out the QOs from the BLG LLs, leaving the MLG LLs resolvable as demonstrated in Extended Data Fig. 2d,e. The largest n^{ac} also enables observation of the paramagnetic response $\partial M/\partial\mu = C/\phi_0$ in the gap between the zeroth and the first MLG LLs dictated by the Chern number $C = 2$ on the electron side and $C = -2$ on the hole side (Extended Data Fig. 2e).

Extended Data Fig. 2f–h shows the QOs at $B_a = 40$ mT, 80 mT and 170 mT. At these low fields, the Dingle broadening greatly suppresses the QOs due to BLG LLs (Extended Data Fig. 4) and reduces the visibility of the MLG LLs at large displacement fields because of the reduction in the gap energies. At 170 mT and $V_{bg}^{ac} = 8$ mV rms, the M2 LLs and the 12-fold degenerate LLs in the gullies are resolved as seen in Extended Data Fig. 2h.

BS calculations

The BS of ABA graphene was calculated in the tight-binding model following refs. 2,36 based on SWMc parameterization[34]. On the basis of $\{A_1, B_1, A_2, B_2, A_3, B_3\}$, where A_i and B_i are the two sublattice sites in the ith layer, the low-energy effective Hamiltonian can be written as

$$H_0 = \begin{pmatrix} \Delta_1+\Delta_2 & v_0\pi^\dagger & v_4\pi^\dagger & v_3\pi & \gamma_2/2 & 0 \\ v_0\pi & \delta+\Delta_1+\Delta_2 & \gamma_1 & v_4\pi^\dagger & 0 & \gamma_5/2 \\ v_4\pi & \gamma_1 & \delta-2\Delta_2 & v_0\pi^\dagger & v_4\pi & \gamma_1 \\ v_3\pi^\dagger & v_4\pi & v_0\pi & -2\Delta_2 & v_3\pi^\dagger & v_4\pi \\ \gamma_2/2 & 0 & v_4\pi^\dagger & v_3\pi & -\Delta_1+\Delta_2 & v_0\pi^\dagger \\ 0 & \gamma_5/2 & \gamma_1 & v_4\pi^\dagger & v_0\pi & \delta-\Delta_1+\Delta_2 \end{pmatrix}$$

where $\Delta_1 = -e(U_1 - U_3)/2$ and $\Delta_2 = -e(U_1 - 2U_2 + U_3)/6$, with U_i the potential of layer i. Δ_1 is determined by the displacement field, whereas Δ_2 describes the asymmetry of the electric field between the layers. The band velocities v_i ($i = 0, 3, 4$) are related to the tight-binding parameters γ_i by $v_i\hbar = \frac{\sqrt{3}}{2}a_c\gamma_i$, where $a_c = 0.246$ nm is the crystal constant of graphene, $\pi = \xi k_x + ik_y$, and ξ is the valley index ($\xi = \pm 1$ for valley K^+ and K^-, respectively).

On a rotated basis $(A_1 - A_3)/\sqrt{2}$, $(B_1 - B_3)/\sqrt{2}$, $(A_1 + A_3)/\sqrt{2}$, B_2, A_2, $(B_1 + B_3)/\sqrt{2}$, the Hamiltonian can be rewritten as

$$H_{TLG} = \begin{pmatrix} \Delta_2-\frac{\gamma_2}{2} & v_0\pi^\dagger & \Delta_1 & 0 & 0 & 0 \\ v_0\pi & \Delta_2+\delta-\frac{\gamma_5}{2} & 0 & 0 & 0 & \Delta_1 \\ \Delta_1 & 0 & \Delta_2+\frac{\gamma_2}{2} & \sqrt{2}v_3\pi & -\sqrt{2}v_4\pi^\dagger & v_0\pi^\dagger \\ 0 & 0 & \sqrt{2}v_3\pi^\dagger & -2\Delta_2 & v_0\pi & -\sqrt{2}v_4\pi \\ 0 & 0 & -\sqrt{2}v_4\pi & v_0\pi^\dagger & \delta-2\Delta_2 & \sqrt{2}\gamma_1 \\ 0 & \Delta_1 & v_0\pi & -\sqrt{2}v_4\pi^\dagger & \sqrt{2}\gamma_1 & \Delta_2+\delta+\frac{\gamma_5}{2} \end{pmatrix}$$

For $\Delta_1 = 0$, the Hamiltonian can be block-diagonalized into MLG-like and BLG-like blocks, that is, $H_{TLG} = H_{MLG} \oplus H_{BLG}$. A finite displacement field hybridizes the two blocks.

In an external magnetic field, in the Landau gauge, the canonical momentum π can be replaced by $\pi - eA$, where A is the vector potential. π obeys the commutation relation $[\pi_x, \pi_y] = -i/l_B$, where $l_B = \sqrt{(\hbar/eB)}$ is the magnetic length. As in the usual one-dimensional harmonic

oscillator, on the basis of LL orbital $|n\rangle$, the matrix elements of π, $\pi^\dagger$ are given by

$$K^+: \pi|n\rangle = \frac{i\hbar}{l_B}\sqrt{2(n+1)}\,|n+1\rangle$$

$$\pi^\dagger|n\rangle = -\frac{i\hbar}{l_B}\sqrt{2n}\,|n-1\rangle$$

$$K^-: \pi|n\rangle = \frac{i\hbar}{l_B}\sqrt{2n}\,|n-1\rangle$$

$$\pi^\dagger|n\rangle = -\frac{i\hbar}{l_B}\sqrt{2(n+1)}\,|n+1\rangle$$

Therefore, the new Hamiltonian can be written on the basis of LL orbitals. Using matrix elements of π and $\pi^\dagger$ operators, the momentum operators are replaced by raising and lowering the diagonal matrix of dimensions $\Lambda \times \Lambda$, where Λ is the cutoff number for the infinite matrix, restricting the Hilbert space with indices $n \le \Lambda$. All the other nonzero elements γ_i are substituted by $\gamma_i I_\Lambda$, where I_Λ is the identity matrix with dimensions $\Lambda \times \Lambda$. As our measurements were performed in low magnetic fields and high-index LLs are often involved, a large cutoff was used so that it spans the energy range significantly larger than in the experiment. We also removed false LLs caused by imposing the cutoff, which usually have very large indices. In the simulations, Λ was set to 400 for small carrier-density ranges (Fig. 2) and to 800 for calculations over larger ranges (Figs. 3 and 4).

Evolution of the BS and LLs with displacement field

Extended Data Fig. 3 shows the calculated BS of ABA graphene using the derived SWMc parameters and the evolution of the LLs with D and B_a. At $D = 0$ ($\Delta_1 = 0$), there is essentially no hybridization between the MLG and BLG bands. All the LLs are valley (and spin) degenerate except for the zeroth LLs of the MLG and BLG bands that are valley polarized because of the Berry curvature (Extended Data Fig. 3a). With increasing Δ_1, the gaps of the MLG and BLG bands increase and the hybridization between the bands grows resulting in the formation of mini-Dirac cones (gullies) and in LL anticrossings (Extended Data Fig. 3b–d). At our highest accessible $\Delta_1 \approx 50$ meV, the lowest LLs in the gullies are well isolated from the rest of the LLs as shown in Extended Data Fig. 3e,f. As the BLG bandgap Δ_G^0 is characterized by $C = 0$, it has no magnetization. The six-fold degenerated compressible zeroth LLs 0_G^+ and 0_G^- in the gullies also have no magnetization at low fields, $M = -\partial\varepsilon/\partial B = 0$, because of their zero kinetic energy. As a result, zero magnetization is observed around the CNP over a width of $\delta n = 12B_a/\phi_0$ in carrier density as indicated in Fig. 2c,f. The first paramagnetic signal appears when the Fermi level reaches the $C = \pm 6$ gaps Δ_G^1 and Δ_G^{-1} between the zeroth and the first gully LLs as shown in Fig. 2f. At elevated magnetic fields, the six-fold gully degeneracy of the zeroth LLs is partially lifted[4,53].

Reconstruction of BS parameters

Several experimental studies[3,4,37,38,40,51,52,54,64] have investigated the tight-binding parameters of ABA graphene as shown in Extended Data Table 1. The high resolution of our data and the fine features attained at low magnetic fields allow high-precision reconstruction of SWMc parameters as follows. We set γ_0 to the standard literature value of 3,100 meV, which corresponds to Fermi velocity of graphene $v_F = \frac{\sqrt{3}}{2\hbar} a_c \gamma_0 = 10^6$ m s^{-1}. The γ_0 sets the overall energy scale, whereas the value of the remaining seven parameters, relative to γ_0, determine the BS. The fitting of the parameters was performed manually. We first determined the effect of the individual parameters on particular features of the BS as shown in Extended Data Fig. 4, which then guided us in the iterative fitting process. In particular, in the absence of displacement field, $\Delta_1 = 0$, the MLG band is affected by only γ_0, γ_2, γ_5 and δ, with the gap at the Dirac point given by $E_g^0 = \delta + \frac{\gamma_2 - \gamma_5}{2}$. The BLG band is strongly dependent on γ_0, γ_1 and γ_3, weakly dependent on γ_4 and essentially independent of γ_5 and δ. The BLG gap size is mainly governed by γ_2 and Δ_2. The relative energy shift between the MLG and BLG bands is mainly governed by γ_2.

The dependence of the measured QOs on n and D at low B_a provides a very sensitive tool for determining the SWMc parameters. After developing an understanding of the influence of the individual parameters on the relative position of the LLs in specific regions in the (n, D) plane, an initial set of parameters was chosen to attain an approximate fit to the data. Then fine-tuning of the parameters is achieved by calculating the QOs for each set of parameters and comparing with the data at $D = 0$ V nm^{-1}. This process is repeated manually adjusting the different parameters in an iterative manner. After attaining a good fit at $D = 0$, additional fine-tuning was performed to fit the entire range of D. As the different parameters have a distinctive effect on the relative positions of the LLs, this manual procedure is readily manageable. The error bars were determined by the values of the individual parameters for which a visible deviation from the data was observed.

The following attributes were particularly informative for the fitting processes:

1. The number of BLG LLs between the adjacent MLG LLs
2. The relative energy shift between MLG and BLG bands
3. LL anticrossings in the gullies
4. The gap size of MLG band

Attribute 1 is determined by the DOS ratio of the two bands, which is predominantly governed by γ_1. By adjusting γ_1 to fit the relative number of BLG and MLG LLs along with optimization of other parameters we obtain $\gamma_1 = 370 \pm 10$ meV.

Attribute 2 is then used to determine γ_2. The energies of the band extrema and hence the relative position of the zeroth LLs can be calculated analytically. In particular, for $\Delta_1 = 0$, the 0_{M1}^- LL at the bottom of M1 band is positioned at energy $\Delta_2 - \gamma_2/2$, whereas the top of BLG valence band is at $\Delta_2 + \gamma_2/2$. Thus, the relative position between MLG and BLG bands is determined by γ_2 and Δ_2. As the LL spectrum is quite sensitive to Δ_2, γ_2 is determined first. We use the relative position between -1_{M3} and the nearby BLG LLs to fit γ_2, and we get $\gamma_2 = -19 \pm 0.5$ meV.

Attribute 3 is governed by γ_3, which induces trigonal warping of the BLG bands. As shown in Extended Data Fig. 6, this results in the anticrossings between the BLG LLs and MLG 0_{M3}^- and -1_{M3}^+ LLs. From fitting to the experimental data, we obtain $\gamma_3 = 315 \pm 10$ meV.

Attributes 2 and 4 are used to derive δ and γ_5. The MLG band gap at $D = 0$ V nm^{-1} is $E_g^0 = \delta + (\gamma_2 - \gamma_5)/2$, whereas the gap centre is located at $2\Delta_2 + \delta - (\gamma_2 + \gamma_5)/2$. In our experimental data, one BLG LL fits within the MLG gap and 20 BLG LLs reside between 0_{M1}^- and -1_{M3}, from which we attain $\delta = 18.5 \pm 0.5$ meV and $\gamma_5 = 20 \pm 0.5$ meV. Note that E_g^0 can be either positive or negative. We find that E_g^0 is negative, which means that the zeroth K^- LL (0_{M1}^-) resides at the bottom of the M1 band and the zeroth K^+ LL (0_{M2}^+) is at the top of M2. In this case, the Dirac gap E_g increases with Δ_1 and the 0_{M1}^- and the 0_{M2}^+ LLs spread apart with the displacement field as shown in Extended Data Fig. 3f, consistent with experimental data in Fig. 2c,e and calculations in Fig. 2d. If E_g^0 is positive, the zeroth K^- LL will reside at the top of M2, whereas the zeroth K^+ LL will be at the bottom of M1. In this case, on increasing D, the Dirac gap closes and then reopens with the crossing of the two zeroth LLs, such that E_g is always negative at high D with zeroth K^- LL at the bottom of M1. Extended Data Table 1 shows that the value and the sign of E_g^0 varies notably in the literature. However, only in ref. 40 and in the present work the Dirac gap is reported directly. For the rest of the references, the E_g^0 values presented in the table are calculated from the reported values of δ, γ_2 and γ_5.

Δ_2 mainly affects the gap of the BLG bands and as -1_{M3} resides closely to the BLG band gap, we use the number of BLG LLs between -1_{M3} and -2_{M3} to fit Δ_2 and get $\Delta_2 = 3.8 \pm 0.05$ meV. γ_4 plays the most negligible role, slightly adjusting the shape of the BLG bands. The fitting procedure is to choose these parameters such that the inaccuracy of the number of BLG LLs between any pair of MLG LLs is no more than one.

By optimizing all parameters for best fit to the experimental data, we derive $\gamma_4 = 140 \pm 15$ meV, as shown in Extended Data Table 1.

Orbital magnetization calculations

Oscillations in orbital magnetization M from the LLs can be calculated analytically for either parabolic or Dirac bands as shown previously[65]. However, there is no analytical expression for the LL spectrum in ABA graphene; therefore, the magnetization oscillations have to be calculated numerically. We follow the method described in ref. 14 to derive the magnetization $M(n)$ and then calculate its derivative $\partial M/\partial n$.

We first consider the case with zero LL broadening. For an arbitrary LL spectrum E_i with degeneracy D_i (i is the Landau-level index), the DOS $N_0(\varepsilon)$ of the system is

$$N_0(\varepsilon) = \sum_i D_i \delta(\varepsilon - E_i).$$

E_i describes spin-degenerate LLs from both valleys with degeneracy $D_i = 2\frac{eB}{h}$. The grand thermodynamic potential $\Omega_0(\mu, B)$ is then given by

$$\Omega_0 = -kT\int_{-\infty}^{\infty} N_0(\varepsilon)\ln(1+e^{[(\mu-\varepsilon)/kT]})\,d\varepsilon,$$

where k is the Boltzmann constant, T is the temperature and μ is the chemical potential.

Now we consider LL broadening of width Γ (Dingle parameter) with a Lorentzian form

$$L(\varepsilon) = \frac{1}{\pi}\left(\frac{\Gamma}{\varepsilon^2+\Gamma^2}\right).$$

The DOS and the grand potential are then described by

$$N(\varepsilon) = \sum_i D_i L(\varepsilon - E_i),$$

$$\begin{aligned}\Omega &= -kT\int_{-\infty}^{\infty} N(\varepsilon)\ln(1+e^{[(\mu-\varepsilon)/kT]})\,d\varepsilon \\ &= -kT\int_{-\infty}^{\infty}\sum_i D_i L(\varepsilon-E_i)\ln(1+e^{[(\mu-\varepsilon)/kT]})\,d\varepsilon.\end{aligned}$$

Then M is given by

$$\begin{aligned}M &= -\frac{\partial\Omega}{\partial B} \\ &= kT\int_{-\infty}^{\infty}\sum_i\left(\frac{\partial D_i}{\partial B}L(\varepsilon-E_i) - D_i L'(\varepsilon-E_i)\frac{\partial E_i}{\partial B}\right)\ln(1+e^{[(\mu-\varepsilon)/kT]})\,d\varepsilon,\end{aligned}$$

where $L'(\varepsilon) = \partial L(\varepsilon)/\partial\varepsilon$. In the zero-temperature limit ($T \to 0$), M can be simplified:

$$M = \int_{-\infty}^{\mu}\sum_i\left(\frac{\partial D_i}{\partial B}L(\varepsilon-E_i) - D_i L'(\varepsilon-E_i)\frac{\partial E_i}{\partial B}\right)(\mu-\varepsilon)\,d\varepsilon.$$

To compare with our experiment, we need to calculate

$$\frac{\partial M}{\partial n}(n) = \frac{\partial M}{\partial \mu}(n)\frac{\partial \mu}{\partial n}(n),$$

where $\frac{\partial\mu}{\partial n}(n)$ is the inverse of the DOS as a function of the carrier density and $n(\mu) = \int_{-\infty}^{\mu} N(\varepsilon)\,d\varepsilon$.

Extended Data Fig. 5 shows the calculated $n(\mu)$, $\frac{\partial n}{\partial \mu}(\mu)$, $\frac{\partial n}{\partial \mu}(n)$, $\frac{\partial M}{\partial \mu}(\mu)$, $\frac{\partial M}{\partial \mu}(n)$ and $\frac{\partial M}{\partial n}(n)$ versus Δ_1 at $B_a = 320$ mT using the derived SWMc parameters and Dingle broadening $\Gamma = 0.3$ meV. The modulation in DOS, $\partial n/\partial\mu$, is well resolved in Extended Data Fig. 5b,c, but it is relatively small because of the LL broadening, except near CNP, in which large gaps with vanishing DOS open between the lowest LLs in the gullies at elevated Δ_1.

The calculated $\partial M/\partial\mu$ versus μ in Extended Data Fig. 5d shows that the crossing of the MLG and BLG LLs does not cause any phase shift. By contrast, in $\partial M/\partial\mu$ versus n in Extended Data Fig. 5e, the BLG LLs show a 2π shift on crossing the four-fold degenerate MLG LLs and a π shift on crossing the two-fold degenerate zeroth LLs. This arises from the fact that the filling an MLG LL delays filling the next BLG LL versus total n, but not versus μ. As the DOS modulation $\frac{\partial n}{\partial\mu}(n)$ is quite small, $\frac{\partial M}{\partial n}(n)$ in Extended Data Fig. 5f looks very similar to $\frac{\partial M}{\partial\mu}(n)$ except near CNP.

Derivation of the Dingle parameter

The energy bands are broadened by the intrinsic broadening Γ, given by the quantum scattering time $\tau_q = \hbar/2\Gamma$. Hence Γ sets the finest meaningful energy resolution with which the band energy can be described. To attain this energy resolution experimentally, we need to use the lowest B_a for which the LL energy gaps are comparable to Γ. In this limit, the amplitude of the QOs is rapidly suppressed with increasing Γ. Extended Data Fig. 4c–g shows the calculated QOs for various Dingle parameters $\Gamma = 0.2$–0.8 meV. As the energy spacing of the BLG LLs in the conduction band is about 1 meV, the amplitude of their QOs is suppressed by about two orders of magnitude over this range of Γ, whereas in the valence band, in which the LL gaps are about 0.6 meV, the QOs are completely quenched with the higher Γ. By contrast, the amplitude of the QOs of the MLG LLs, which have an order of magnitude larger gaps at low carrier densities, is much less affected by these Γ values. As a result, the relative amplitude of the MLG and BLG QOs is strongly dependent on Γ, enabling its accurate determination. By fitting to the experimental data in Fig. 2, we obtain $\Gamma = 0.3 \pm 0.05$ meV, which also provides a very good agreement in quantitative comparison between the amplitudes of the measured B_z^{ac} and the calculated m_z taking into account the 2D magnetization reconstruction.

The finite n^{ac} modulation by V_{bg}^{ac} also causes a suppression of the apparent amplitude of the QOs. It can be shown that if the peak-to-peak value of the carrier-density modulation is less than half of the LL degeneracy, $n^{ac} < 2B_a/\phi_0$, which is the case in our high-resolution measurements, the suppression is less than a factor of π/2. For larger n^{ac}, the visibility is suppressed rapidly as shown in Extended Data Fig. 2d,e. In particular, in Figs. 3 and 4 we have intentionally used larger n^{ac} to suppress the QOs due to BLG LLs and to improve the signal-to-noise ratio for detections of the MLG LLs. As this type of suppression of the apparent amplitude of QOs is harder to simulate in our BS calculations, we have used $\Gamma = 0.3$ meV for the calculations presented in all the figures except in Figs. 3 and 4, where $\Gamma = 0.6$ meV was used instead for suppression of the BLG QOs artificially. This larger Γ does not affect the shape of the calculated MLG QOs appreciably but reduces their amplitude.

Our derived $\Gamma = 0.3$ meV with corresponding local quantum scattering time $\tau_q = \hbar/2\Gamma \approx 1$ ps, is about four times lower than the value reported based on global SdH oscillations[40]. This is consistent with the observation that the lowest magnetic field for detection of QOs in our local dHvA measurements is substantially lower than what is required for detection of the SdH oscillations (Extended Data Fig. 1). The large Γ reported based on SdH oscillations is probably because of sample inhomogeneity, such as charge disorder and the PMFs (B_S). Hence, the measurement of the local dHvA QOs enables the determination of the local BS with energy resolution set by the intrinsic broadening Γ of the energy bands. This is of key importance for the study of BS of twisted vdW materials that are particularly prone to strain and spatial inhomogeneities.

LL anticrossings

The hybridization between the BLG and MLG bands on increasing Δ_1 with the displacement field gives rise to partial lifting of valley degeneracy of the LLs. This effect is particularly pronounced near the top of the BLG valence band at intermediate values of Δ_1 as shown in Extended

Data Fig. 6c,d. Here, when MLG and BLG LLs in the same valley intersect, the strong band hybridization and non-vanishing γ_3 leads to avoided crossing between the LLs as marked by the open symbols. Interestingly, the anticrossing occurs between the MLG LLs and every third BLG LL. Our derived SWMc parameters provide an excellent fit to the experimentally observed anticrossings as demonstrated in Extended Data Fig. 6a,b. Moreover, the strong hybridization lifts the valley degeneracy of the first MLG LL in the M3 sector as shown by the pronounced splitting between -1^{-}_{M3} and -1^{+}_{M3} in Extended Data Fig. 6b–d. This splitting is resolved experimentally in Extended Data Fig. 6a.

Interference of BLG LLs

The interference of the LLs can be observed also in the BLG bands at the same locations at which it is present in the MLG bands. Extended Data Fig. 7 shows the QOs acquired at site B as in Figs. 3h and 4e, but using lower $V^{ac}_{bg} = 8$ mV rms that enables resolving the BLG LLs. The beating nodes at around 0.5×10^{12} cm^{-2}and 1.8×10^{12} cm^{-2} are seen (Extended Data Fig. 7b), which can be well reproduced by the simulations using $B_S = 4.2$ mT (Extended Data Fig. 7c).

Resolution of the PMF by LL interference

The minimal PMF that can be measured using the interference method is determined by the highest accessible LL index of the beating node N^1_b. At $B_a = 320$ mT in the accessible range of n, the highest MLG LL index in ABA graphene is ±70, and hence the minimal $B_S = B_a/(4N^1_b) = 1.14$ mT. For comparison, the lowest PMF that has been recently resolved by scanning tunnelling microscope is $B_S \approx 0.5$ T (ref. 66).

PMFs on different length scales

In moiré 2D materials, notable lattice relaxation occurs, giving rise to periodic strain and PMFs up to tens of tesla within moiré unit cell[67–69]. This short-range periodic PMF is part of the periodic potential that determines the BS[70,71], but does not affect the usual LLs. By contrast, the strain that we probe varies gradually on a much larger length scale (about 1 μm). This strain gives rise to smooth PMFs, which shift the LLs in the presence of B_a and form strain-induced LLs at zero magnetic field[6,72–75].

Towards characterization and use of PMFs

Strain engineering has been proposed to realize programmable PMFs leading to topological phases and various electronic devices[5,48]. Although large, short-range PMFs have been widely observed[6,7,67–69,72–75], long-range homogeneous and controllable PMFs required for the development of new functionalities and valleytronics have not been realized[5,43,44]. Several methods have been proposed to induce variable mesoscale strain, including bending, MEMS, piezoelectric devices and polyimide deformation[47,76–79], but the generated PMFs could not be detected. Our method enables the integration of such in situ controllable strain engineering, transport measurements and high-resolution local PMF imaging, laying the groundwork for investigation and use of PMFs.

Discussion of possible alternative mechanisms of interference of QOs

We consider below several other possible mechanisms that can alter the BS and induce degeneracy lifting, which may lead to interference of the LLs, and show that they are incompatible with the experimental data.

Band shifting. Spin–orbit coupling as well as the Zeeman effect at elevated fields can lift flavour degeneracy producing an energy shift between the bands of opposite spin or valley. Both the intrinsic spin–orbit coupling in graphene and the Zeeman contributions at our low magnetic fields result in a negligible energy shift of the order of μeV (refs. 80,81), which cannot account for the experimental data. Nevertheless, we explore whether a generic rigid shift between bands can reproduce the revealed LL interference pattern. In Fig. 3h, the first node in the interference of the MLG LLs occurs at an index $N \approx 19$. The corresponding LL energy gap is $\Delta E_N = E_{N+1} - E_N = \sqrt{2e\hbar v_F^2 B_a}\,(\sqrt{N+1} - \sqrt{N}) \approx 2.5$ meV. For the destructive interference, the LLs of the two bands have to be out of phase, namely, shifted by $\delta E_N \approx 1.25$ meV. Extended Data Fig. 8a shows the BS with a rigid shift of 1.25 meV between the K^+ and K^- bands with the corresponding calculated QOs presented in Extended Data Fig. 8b. The main resulting feature is that the MLG LLs are split into two, which is markedly different from the experimental QOs. This points out that to reproduce the observed QOs, the energy shift δE_N between the interfering LLs has to grow with the LL index rather than being constant or decreasing with N. This is the behaviour in the case of PMF, where $\delta E_N = \sqrt{2e\hbar v_F^2 N}\,(\sqrt{B_a + B_S} - \sqrt{B_a - B_S}) \approx B_S\sqrt{2e\hbar v_F^2 N/B_a}$ grows as $\sqrt{N}$.

Staggered substrate potential. The possible alignment between the hBN and ABA graphene can cause an on-site potential difference between the A and B sublattices. Here we consider the simplest situation in which one of the graphene layers (bottom) is aligned with the hBN giving rise to a staggered substrate potential. In this case, the Hamiltonian can be written on the basis of $\{A_1, B_1, A_2, B_2, A_3, B_3\}$ as

$$H_0 = \begin{pmatrix} \Delta_1 + \Delta_2 & v_0\pi^\dagger & v_4\pi^\dagger & v_3\pi & \gamma_2/2 & 0 \\ v_0\pi & \delta + \Delta_1 + \Delta_2 & \gamma_1 & v_4\pi^\dagger & 0 & \gamma_5/2 \\ v_4\pi & \gamma_1 & \delta - 2\Delta_2 & v_0\pi^\dagger & v_4\pi & \gamma_1 \\ v_3\pi^\dagger & v_4\pi & v_0\pi & -2\Delta_2 & v_3\pi^\dagger & v_4\pi \\ \gamma_2/2 & 0 & v_4\pi^\dagger & v_3\pi & -\Delta_1 + \Delta_2 + \delta_{A3} & v_0\pi^\dagger \\ 0 & \gamma_5/2 & \gamma_1 & v_4\pi^\dagger & v_0\pi & \delta - \Delta_1 + \Delta_2 + \delta_{B3} \end{pmatrix}.$$

For concreteness, we choose $\delta_{A3} = 2$ meV and $\delta_{B3} = -2$ meV. The resulting BS is shown in Extended Data Fig. 8c (red) in comparison with the original BS (black). The staggered substrate potential increases the gaps of the MLG and BLG bands but does not lift the valley degeneracy and therefore does not lead to beating. Extended Data Fig. 8d presents the calculated QOs showing no LL beating.

Kekulé distortion. Kekulé distortions are the bond density waves that have been observed in graphene epitaxially grown on copper[82] or in the presence of strain[83]. In contrast to the O-type Kekulé distortion that opens a gap at the Dirac point, we find that the Y-type[84] distortion can result in LL interference. The Y-shaped modulation of the bond strength, parametrized by the hopping parameters γ_0 and γ'_0 (Extended Data Fig. 8e), gives rise to valley-momentum locking and to inequivalent Fermi velocities for both the MLG and BLG bands. Hence, it lifts the valley degeneracy of the LLs resulting in chiral symmetry breaking. In the SWMc model, γ_0 is the sole parameter that controls the Fermi velocity v_F of the MLG band ($v_F = \frac{\sqrt{3}}{2}\frac{a\gamma_0}{\hbar}$). The energy difference between the LLs from the two valleys with the same index N is $\delta E_N = \sqrt{2e\hbar N B_a}\,\Delta v_F$, where $\Delta v_F = \frac{\sqrt{3}}{2}\frac{a}{\hbar}(\gamma_0 - \gamma'_0)$. The first beating node appears when δE_n is equal to half of the gap size: $\sqrt{2e\hbar N B_a}\,\Delta v_F = \sqrt{e\hbar v_F^2 B_a/2N}/2$, which yields $N^1_b = v_F/(4\Delta v_F)$ as shown in Extended Data Fig. 8f. In Fig. 3h, $N^1_b = 19$, which corresponds to a very weak Kekulé distortion with $\Delta v_F/v_F = 1.4 \times 10^{-2}$. However, the Kekulé distortion results in N^1_b that is independent of B_a as corroborated by the calculated QOs for $B_a = 320$ mT and 170 mT in Extended Data Fig. 8h,i. This is because the LLs shift in the same proportion in the two valleys with B_a. This is in sharp contrast to beating due to PMF for which $N^1_b = B_a/(4B_S)$ is proportional to B_a. The experimental data points in Extended Data Fig. 8g (circles) are consistent with PMF and incompatible with the Kekulé distortion.

Disorder in BS parameters. The BS can vary in space because of various types of disorder. Focusing on the Dirac bands, for example, the energy of the Dirac point or v_F could be position dependent without breaking the valley symmetry. If the parameters change gradually in

space on lengths scale larger than our spatial resolution of about 150 nm, the LLs will shift gradually in space following the variations in the BS without showing interference at any location. Let us now consider the opposite case of sharp boundaries between domains with different BS. In this situation, at the boundaries, the finite size of our SOT may result in the simultaneous detection of LLs originating from the two neighbouring domains giving rise to apparent interference. In such a case, we expect to observe interference along a network of grain boundaries with width comparable to our SOT size. Instead, Fig. 3e shows well-defined domains of typical width of 1 μm and length of up to 2 μm, much larger than the SOT size, over which the interference is rather uniform. Furthermore, most of the domains showing beating are located at the ends or corners of the device, so they do not have two neighbouring domains that can cause the apparent interference. Finally, if there is a relative shift in the Dirac point between the neighbouring domains, the apparent interference patterns at the boundary would evolve similar to that calculated in Extended Data Fig. 8b, whereas if v_F changes between the domains the beating node N_b^1 of the apparent interference would be independent of B_a as calculated in Extended Data Figs. 8f–i. Both these possibilities are inconsistent with the experimental data. More generally, the B_a dependence of the LL interference due to variations in BS is distinctly different from the one caused by B_S. We therefore conclude that disorder that causes spatial variations in BS without creating PMFs cannot explain the observed LL interference.

Data availability

The data that support the findings of this study are available from the corresponding authors on reasonable request.

Code availability

The BS calculations codes used in this study are available from the corresponding authors on reasonable request.

49. Hao, Y. et al. Probing layer number and stacking order of few-layer graphene by Raman spectroscopy. *Small* **6**, 195–200 (2010).
50. Jain, A. et al. Minimizing residues and strain in 2D materials transferred from PDMS. *Nanotechnology* **29**, 265203 (2018).
51. Shimazaki, Y. et al. Landau level evolution driven by band hybridization in mirror symmetry broken ABA-stacked trilayer graphene. Preprint at https://doi.org/10.48550/arXiv.1611.02395 (2016).
52. Datta, B. et al. Strong electronic interaction and multiple quantum Hall ferromagnetic phases in trilayer graphene. *Nat. Commun.* **8**, 14518 (2017).
53. Winterer, F. et al. Spontaneous gully-polarized quantum Hall states in ABA trilayer graphene. *Nano Lett.* **22**, 3317–3322 (2022).
54. Stepanov, P. et al. Tunable symmetries of integer and fractional quantum Hall phases in heterostructures with multiple Dirac bands. *Phys. Rev. Lett.* **117**, 076807 (2016).
55. Datta, B. et al. Nontrivial quantum oscillation geometric phase shift in a trivial band. *Sci. Adv.* **5**, eaax6550 (2019).
56. Henriksen, E. A., Nandi, D. & Eisenstein, J. P. Quantum Hall effect and semimetallic behavior of dual-gated ABA-stacked trilayer graphene. *Phys. Rev. X* **2**, 011004 (2012).
57. Zhou, H. et al. Scanning SQUID-on-tip microscope in a top-loading cryogen-free dilution refrigerator. *Rev. Sci. Instrum.* **94**, 053706 (2023).
58. Finkler, A. et al. Self-aligned nanoscale SQUID on a tip. *Nano Lett.* **10**, 1046–1049 (2010).
59. Anahory, Y. et al. SQUID-on-tip with single-electron spin sensitivity for high-field and ultra-low temperature nanomagnetic imaging. *Nanoscale* **12**, 3174–3182 (2020).
60. Huber, M. E. et al. DC SQUID series array amplifiers with 120 MHz bandwidth. *IEEE Trans. Appl. Supercond.* **11**, 1251–1256 (2001).
61. Finkler, A. et al. Scanning superconducting quantum interference device on a tip for magnetic imaging of nanoscale phenomena. *Rev. Sci. Instrum.* **83**, 073702 (2012).
62. Halbertal, D. et al. Nanoscale thermal imaging of dissipation in quantum systems. *Nature* **539**, 407–410 (2016).
63. Meltzer, A. Y., Levin, E. & Zeldov, E. Direct reconstruction of two-dimensional currents in thin films from magnetic-field measurements. *Phys. Rev. Applied* **8**, 064030 (2017).
64. Asakawa, Y. et al. Intersubband Landau level couplings induced by in-plane magnetic fields in trilayer graphene. *Phys. Rev. Lett.* **119**, 186802 (2017).
65. Shoenberg, D. Magnetization of a two-dimensional electron gas. *J. Low Temp. Phys.* **56**, 417–440 (1984).
66. Li, S.-Y., Su, Y., Ren, Y.-N. & He, L. Valley polarization and inversion in strained graphene via pseudo-Landau levels, valley splitting of real Landau levels, and confined states. *Phys. Rev. Lett.* **124**, 106802 (2020).
67. Shi, H. et al. Large-area, periodic, and tunable intrinsic pseudo-magnetic fields in low-angle twisted bilayer graphene. *Nat. Commun.* **11**, 371 (2020).
68. Liu, Y. et al. Tailoring sample-wide pseudo-magnetic fields on a graphene–black phosphorus heterostructure. *Nat. Nanotechnol.* **13**, 828–834 (2018).
69. Zheng, Q. et al. Tunable sample-wide electronic kagome lattice in low-angle twisted bilayer graphene. *Phys. Rev. Lett.* **129**, 076803 (2022).
70. Nam, N. N. T. & Koshino, M. Lattice relaxation and energy band modulation in twisted bilayer graphene. *Phys. Rev. B* **96**, 075311 (2017).
71. Kang, J. & Vafek, O. Pseudomagnetic fields, particle-hole asymmetry, and microscopic effective continuum Hamiltonians of twisted bilayer graphene. *Phys. Rev. B* **107**, 075408 (2023).
72. Ma, C. et al. Landau quantization of a narrow doubly-folded wrinkle in monolayer graphene. *Nano Lett.* **18**, 6710–6718 (2018).
73. Guo, D. et al. Observation of Landau levels in potassium-intercalated graphite under a zero magnetic field. *Nat. Commun.* **3**, 1068 (2012).
74. Yan, W. et al. Strain and curvature induced evolution of electronic band structures in twisted graphene bilayer. *Nat. Commun.* **4**, 2159 (2013).
75. Nigge, P. et al. Room temperature strain-induced Landau levels in graphene on a wafer-scale platform. *Sci. Adv.* **5**, eaaw5593 (2019).
76. Ho, S.-C. et al. Hall effects in artificially corrugated bilayer graphene without breaking time-reversal symmetry. *Nat. Electron.* **4**, 116–125 (2021).
77. Cenker, J. et al. Reversible strain-induced magnetic phase transition in a van der Waals magnet. *Nat. Nanotechnol.* **17**, 256–261 (2022).
78. Wang, L. et al. In situ strain tuning in hBN-encapsulated graphene electronic devices. *Nano Lett.* **19**, 4097–4102 (2019).
79. Pérez Garza, H. H., Kievit, E. W., Schneider, G. F. & Staufer, U. Controlled, reversible, and nondestructive generation of uniaxial extreme strains (>10%) in graphene. *Nano Lett.* **14**, 4107–4113 (2014).
80. Sichau, J. et al. Resonance microwave measurements of an intrinsic spin-orbit coupling gap in graphene: a possible indication of a topological state. *Phys. Rev. Lett.* **122**, 046403 (2019).
81. Banszerus, L. et al. Observation of the spin-orbit gap in bilayer graphene by one-dimensional ballistic transport. *Phys. Rev. Lett.* **124**, 177701 (2020).
82. Gutiérrez, C. et al. Imaging chiral symmetry breaking from Kekulé bond order in graphene. *Nat. Phys.* **12**, 950–958 (2016).
83. Eom, D. & Koo, J.-Y. Direct measurement of strain-driven Kekulé distortion in graphene and its electronic properties. *Nanoscale* **12**, 19604–19608 (2020).
84. Gamayun, O. V., Ostroukh, V. P., Gnezdilov, N. V., Adagideli, İ. & Beenakker, C. W. J. Valley-momentum locking in a graphene superlattice with Y-shaped Kekulé bond texture. *New J. Phys.* **20**, 023016 (2018).

Acknowledgements We thank M. Bocarsly, Y. Liu and B. Han for their discussions. This work was co-funded by the Minerva Foundation (grant no. 140687), the United States–Israel Binational Science Foundation (BSF) (grant no. 2022013) and the European Union (ERC, MoireMultiProbe 101089714). Views and opinions expressed are, however, only ours and do not necessarily reflect those of the European Union or the European Research Council. Neither the European Union nor the granting authority can be held responsible for them. E.Z. acknowledges the support of the Andre Deloro Prize for Scientific Research, the Goldfield Family Charitable Trust and the Leona M. and Harry B. Helmsley Charitable Trust (grant no. 2112-04911). K.W. and T.T. acknowledge support from the JSPS KAKENHI (grant nos 20H00354, 21H05233 and 23H02052) and the World Premier International Research Center Initiative (WPI), MEXT, Japan.

Author contributions H.Z. and N.A. developed the setup and performed the scanning measurements. M.U. and W.Z. fabricated the devices and measured the transport. H.Z., Y.Z. and B.Y. conducted the tight-binding calculation and parameter fitting. N.B. and Y.M. fabricated the SOTs and tuning fork assembly. M.E.H. designed and built the SOT readout system. H.Z., N.A. and M.U. performed the data analysis. H.Z., N.A., M.U. and E.Z. wrote the paper with contributions from the rest of the authors. K.W. and T.T. provided the hBN crystals.

Competing interests The authors declare no competing interests.

Additional information

Correspondence and requests for materials should be addressed to Eli Zeldov.

Peer review information *Nature* thanks Martino Poggio and the other, anonymous, reviewer(s) for their contribution to the peer review of this work.

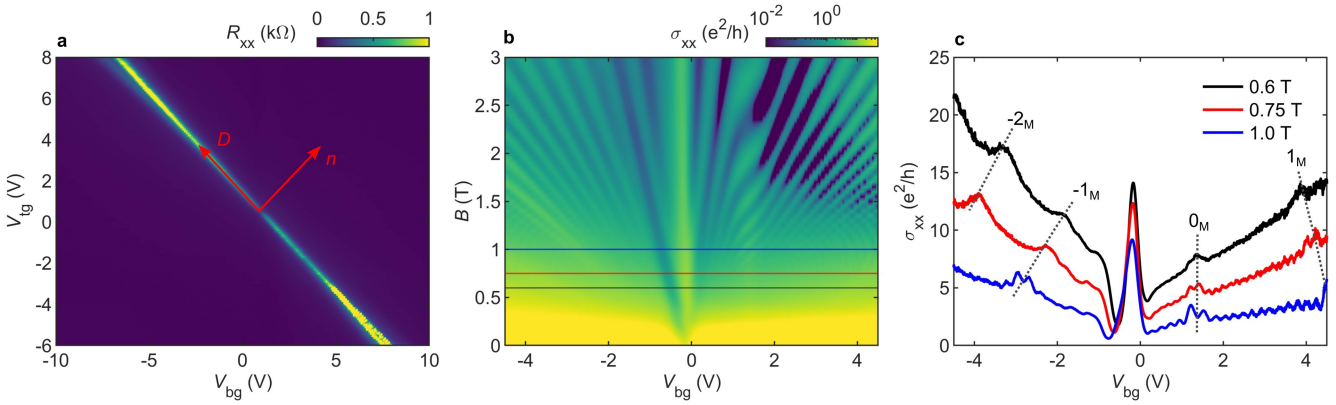

Extended Data Fig. 1 | Transport characterization of ABA graphene. **a**, A dual-gate sweep measurement of R_{xx} at $T = 200$ mK in $B_a = 0$ T in device A described in the main text. **b**, The Landau fan of σ_{xx} in device B at $T = 1.67$ K. **c**, The Shubnikov–de Haas oscillations in σ_{xx} at 0.6, 0.75 and 1.0 T along the lines marked in **b** with indicated MLG LLs. The BLG LLs are visible only at $B_a \gtrsim 0.75$ T for electron doping.

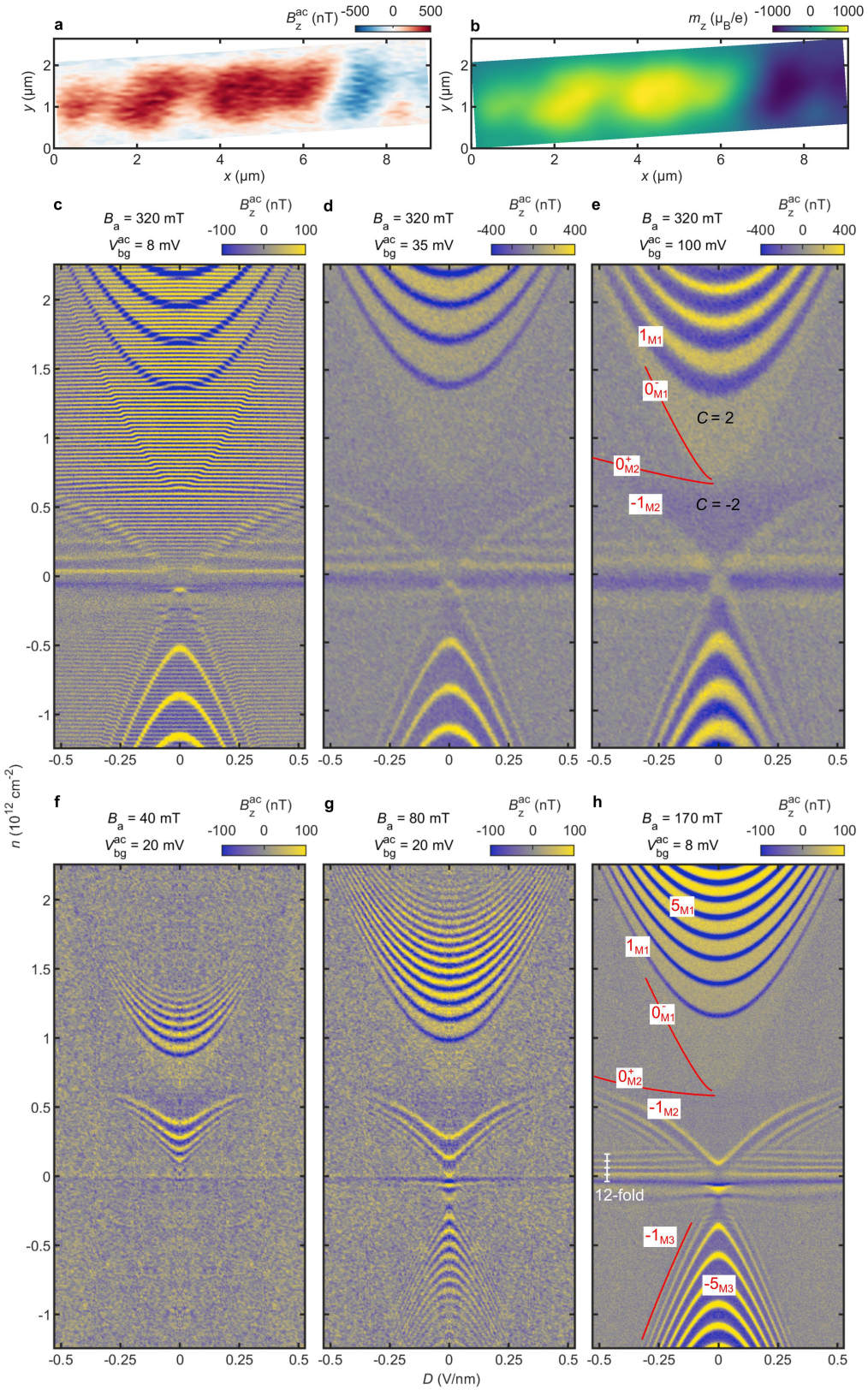

Extended Data Fig. 2 | See next page for caption.

Extended Data Fig. 2 | Reconstruction of the local magnetization from $B_z^{ac}(x,y)$ and comparison of $B_z^{ac}(n,D)$ at different magnetic fields and V_{bg}^{ac}. **a**, Example of the measured $B_z^{ac}(x,y)$ at $n = 5.16\times10^{12}$ cm^{-2}, $B_a = 320$ mT, and $V_{bg}^{ac} = 10$ mV rms. **b**, Differential magnetization $m_z = \partial M/\partial n$ reconstructed from **a**. **c**, The measured QOs at $B_a = 320$ mT and $V_{bg}^{ac} = 8$ mV rms. The induced peak-to-peak carrier density modulation, $n^{ac} = 1.47\times10^{10}$ cm^{-2}, is about half of the LL degeneracy $4B_a/\phi_0$ allowing clear resolution of the BLG and MLG LLs. **d**, QOs at $B_a = 320$ mT and $V_{bg}^{ac} = 35$ mV rms. The BLG LLs are washed out by the large carrier modulation while MLG LLs and the 12-fold degenerate LLs in the gullies are well resolved. **e**, At $V_{bg}^{ac} = 100$ mV rms the MLG QOs are smeared out. The paramagnetic response in the MLG LL gaps with Chern numbers $C = \pm 2$ are clearly visible as indicated. **f**, QOs at $B_a = 40$ mT and $V_{bg}^{ac} = 20$ mV rms. At this low field most of the LLs are smeared by the intrinsic LL broadening and only the lowest MLG LLs in sections M1 and M2 can be resolved at low displacement fields. **g**, Same as **f** at $B_a = 80$ mT. **h**, At $B_a = 170$ mT and $V_{bg}^{ac} = 8$ mV rms the BLG LLs cannot be resolved, but all the MLG LLs and the 12-fold degenerate LLs in the gullies are very prominent.

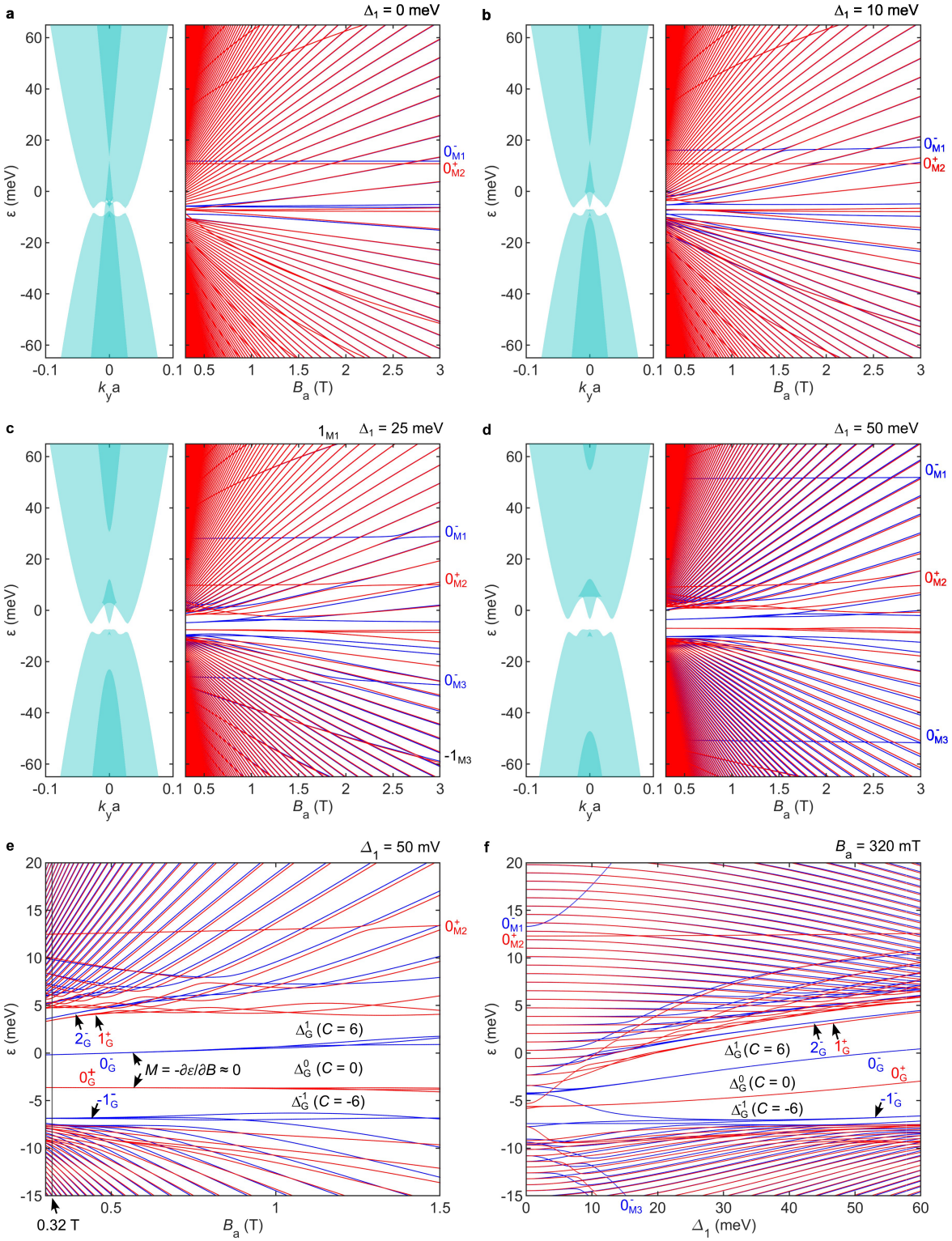

Extended Data Fig. 3 | Evolution of ABA graphene band structure with displacement field. a–**d**, Projected 3D band structure of ABA graphene (left panels) and the corresponding evolution of LLs with B_a at $\Delta_1 = 0, 10, 25$, and 50 meV (right panels). Red and blue lines denote the LLs in K^+ and K^- valleys respectively. The tight-binding parameters used for the calculations are given in Extended Data Table 1 (bottom row). With increasing Δ_1, the MLG and BLG bandgaps grow and band hybridization is enhanced forming mini-Dirac cones (gullies) near CNP. **e**, Zoomed-in view of the evolution of LLs with B_a at $\Delta_1 = 50$ meV. At low fields the zeroth LLs 0_G^+ and 0_G^- are six-fold degenerate (including spin) and have vanishing magnetization. The six-fold degeneracy of the gully LLs is partially lifted at high B_a. The Chern numbers C in the large gaps are indicated. **f**, Evolution of LLs with Δ_1 at $B_a = 320$ mT.

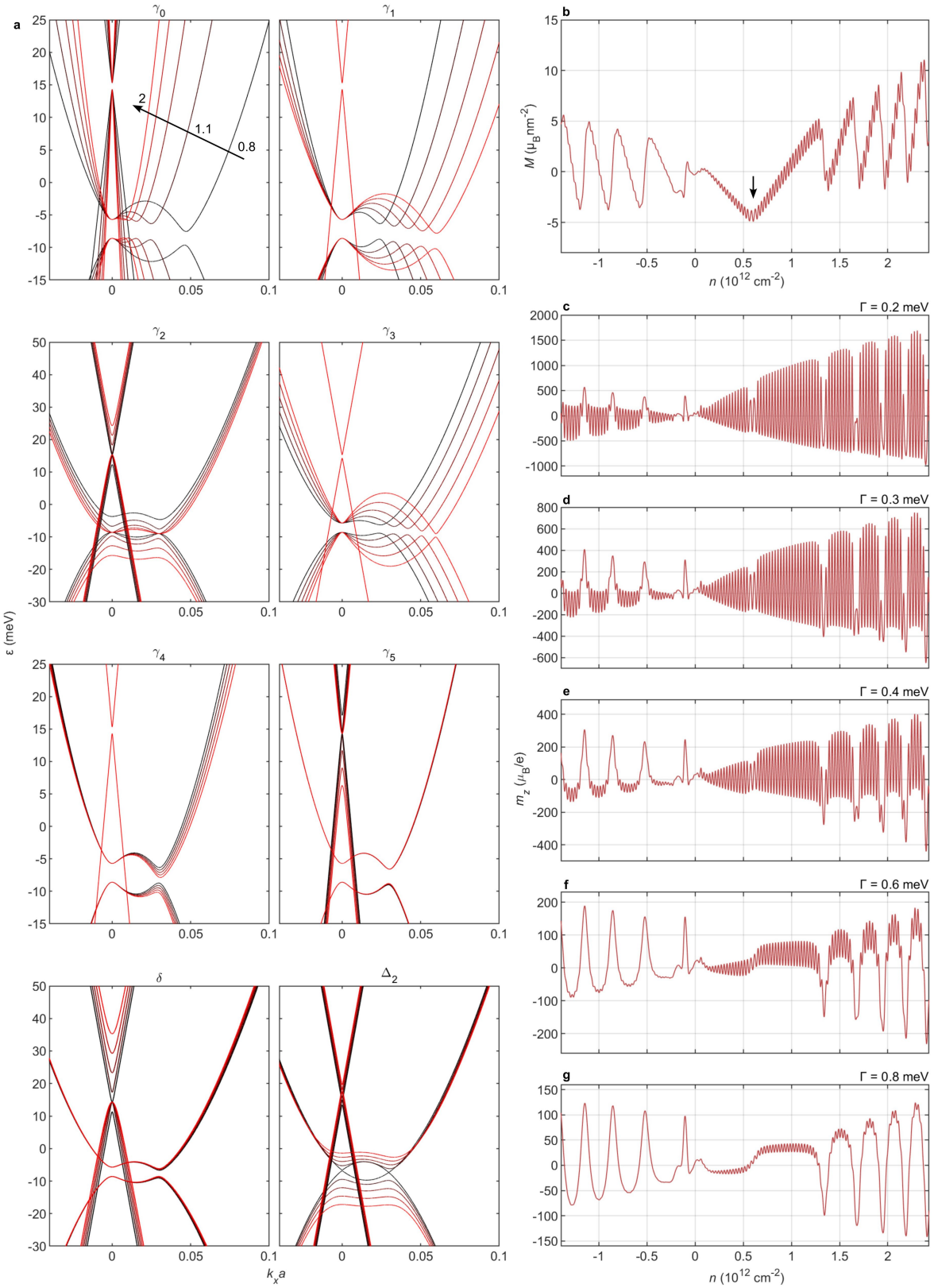

Extended Data Fig. 4 | The dependence of the band structure on the SWMc parameters γ_0 to γ_5, δ, and Δ_2 at $\Delta_1 = 0$ and suppression of QOs by LL broadening. **a**, The effect of individual parameters on the BS, calculated using the parameters of ref. 40 (see Extended Data Table 1) and multiplied by a factor 0.8, 1.1, 1.4, 1.7 and 2 denoted by the different colors from black to red. **b**, Calculated M (n) at $D = 0$ V nm^{-1}, $B_a = 320$ mT, and Dingle parameter $\Gamma = 0.3$ meV. The V-shaped dip in M (black arrow) corresponds to the McClure peak at the Dirac point of the MLG band[14]. **c**–**g**, Calculated differential magnetization $m_z = \partial M / \partial n$ for different $\Gamma = 0.2$ to 0.8 meV. The QOs due to BLG LLs with small energy gaps are suppressed much stronger by Γ than the MLG LLs with large gaps.

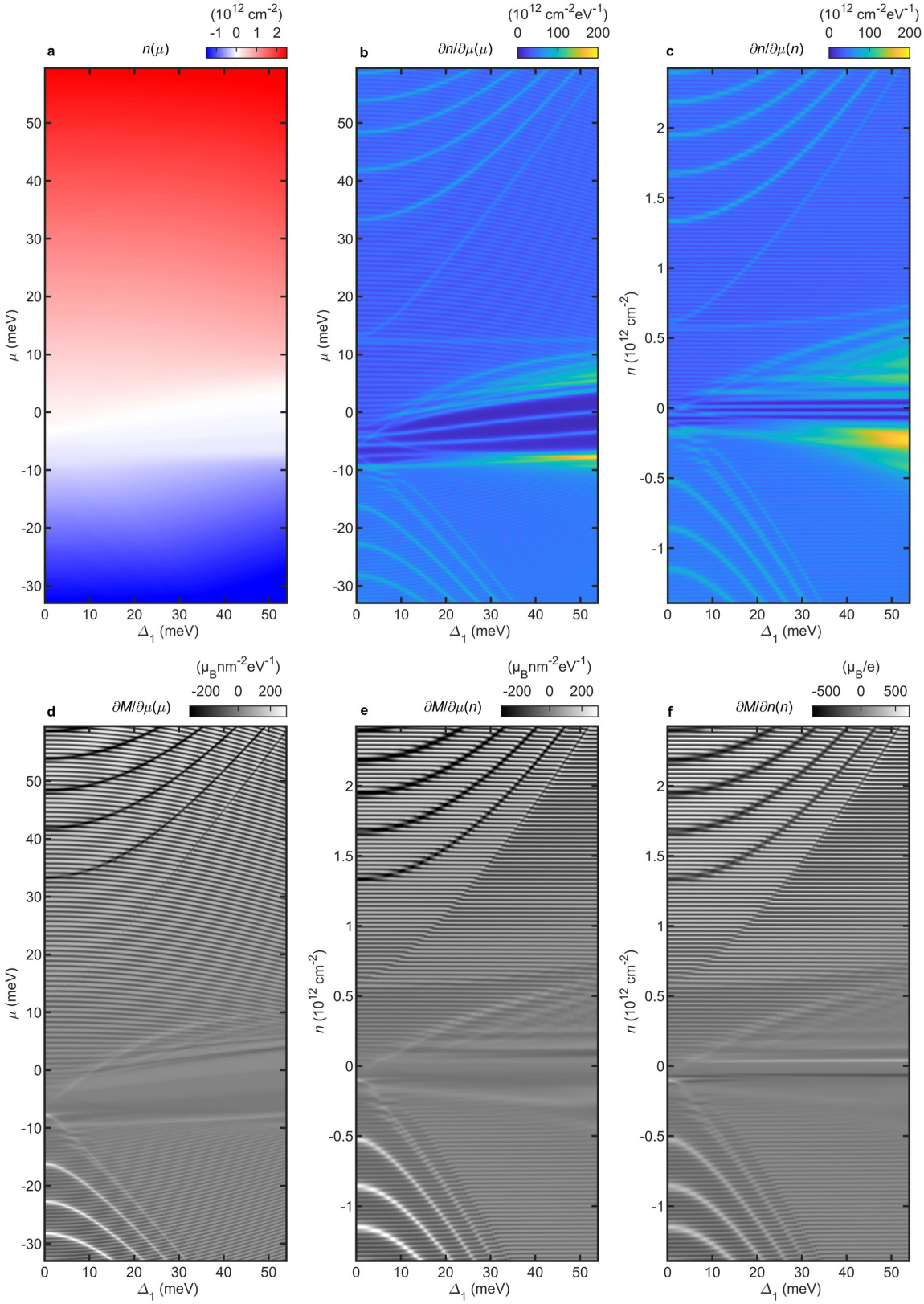

Extended Data Fig. 5 | Calculations of the orbital magnetization. a, Calculated carrier density n as a function of chemical potential μ and displacement-field-induced potential difference Δ_1. **b**, $\partial n/\partial\mu$ versus μ and Δ_1. **c**, $\partial n/\partial\mu$ versus n and Δ_1. **d**, Calculated differential magnetization $\partial M/\partial\mu$ versus μ. **e**,**f**, Calculated $\partial M/\partial\mu$ (**e**) and differential magnetization $m_z = \partial M/\partial n$ (**f**) versus n. $B_a = 320$ mT and $\Gamma = 0.3$ meV in all the calculations.

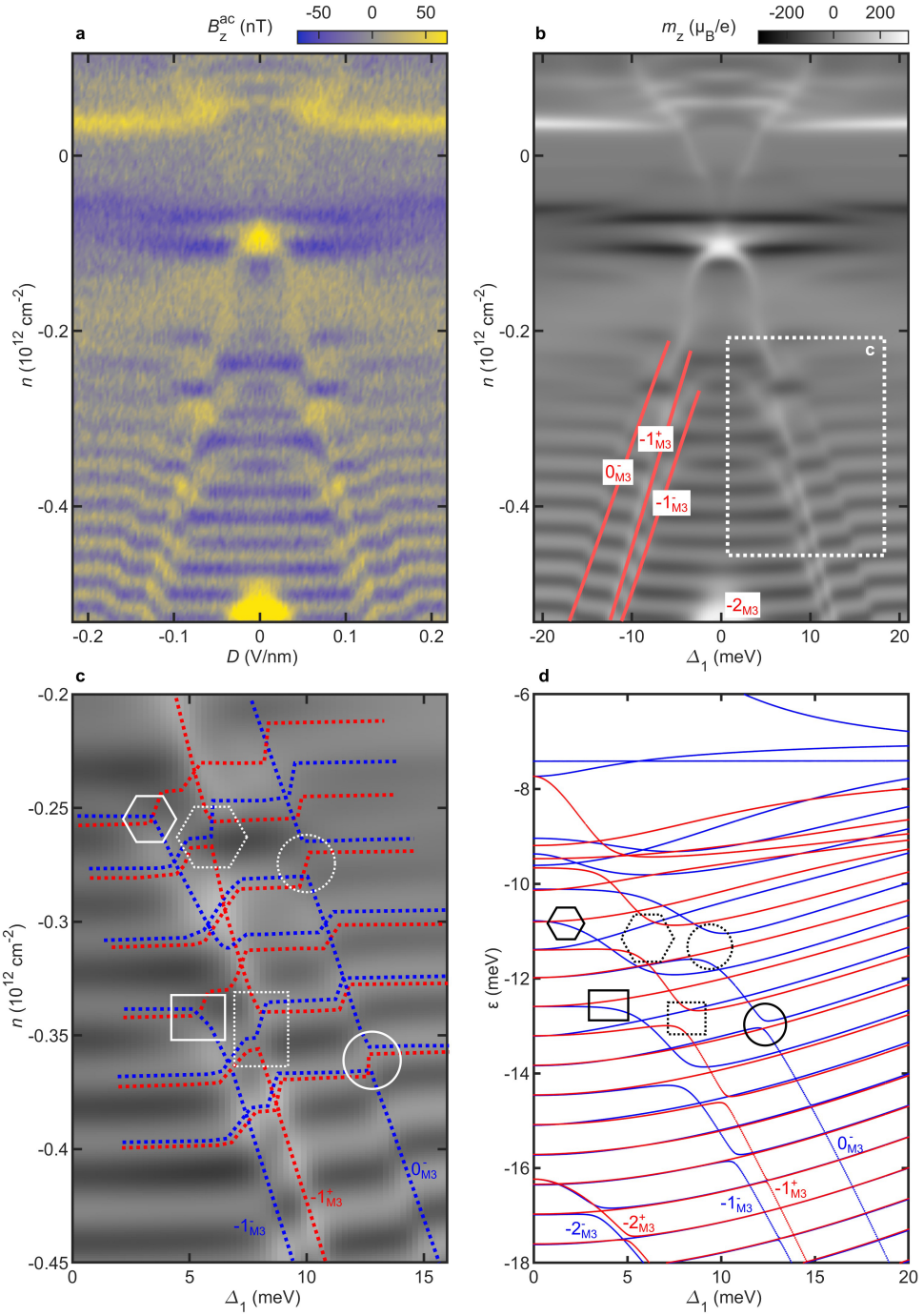

Extended Data Fig. 6 | Landau level anticrossings. a, Measured QOs in B_z^{ac} versus n and D at B_a = 320 mT near the top of the BLG valence band reproduced from Fig. 2f. **b**, Calculated m_z using the derived SWMc parameters providing an excellent fit to the experimental data. **c**, A zoom-in of the region marked in **b** with overlaid schematic LLs. **d**, Calculated LLs in the K^- (blue) and K^+ (red) valleys. The open symbols denote the points of valley splitting and LL anticrossings between the MLG and BLG LLs. The splitting of -1_{M3} LL into valley polarized -1^-_{M3} and -1^+_{M3} LLs is clearly resolved in calculations and in the experimental data.

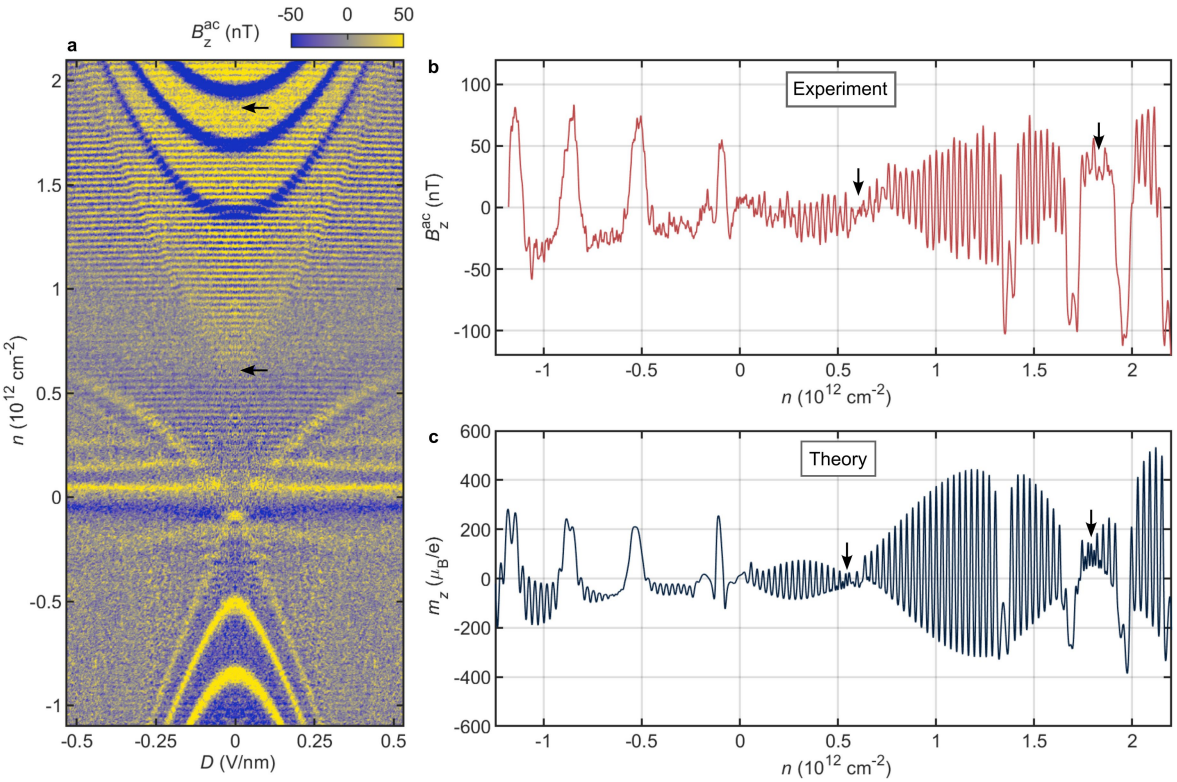

Extended Data Fig. 7 | Beating of the BLG LLs. a, QOs versus n and D at B_a = 320 mT acquired at site B in Fig. 3b using V_{bg}^{ac} = 8 mV rms. **b**, B_z^{ac} versus n profile at D = 0 V nm^{-1}. **c**, Calculated QOs with B_S = 4.2 mT. The black arrows indicate the positions of the beating nodes.

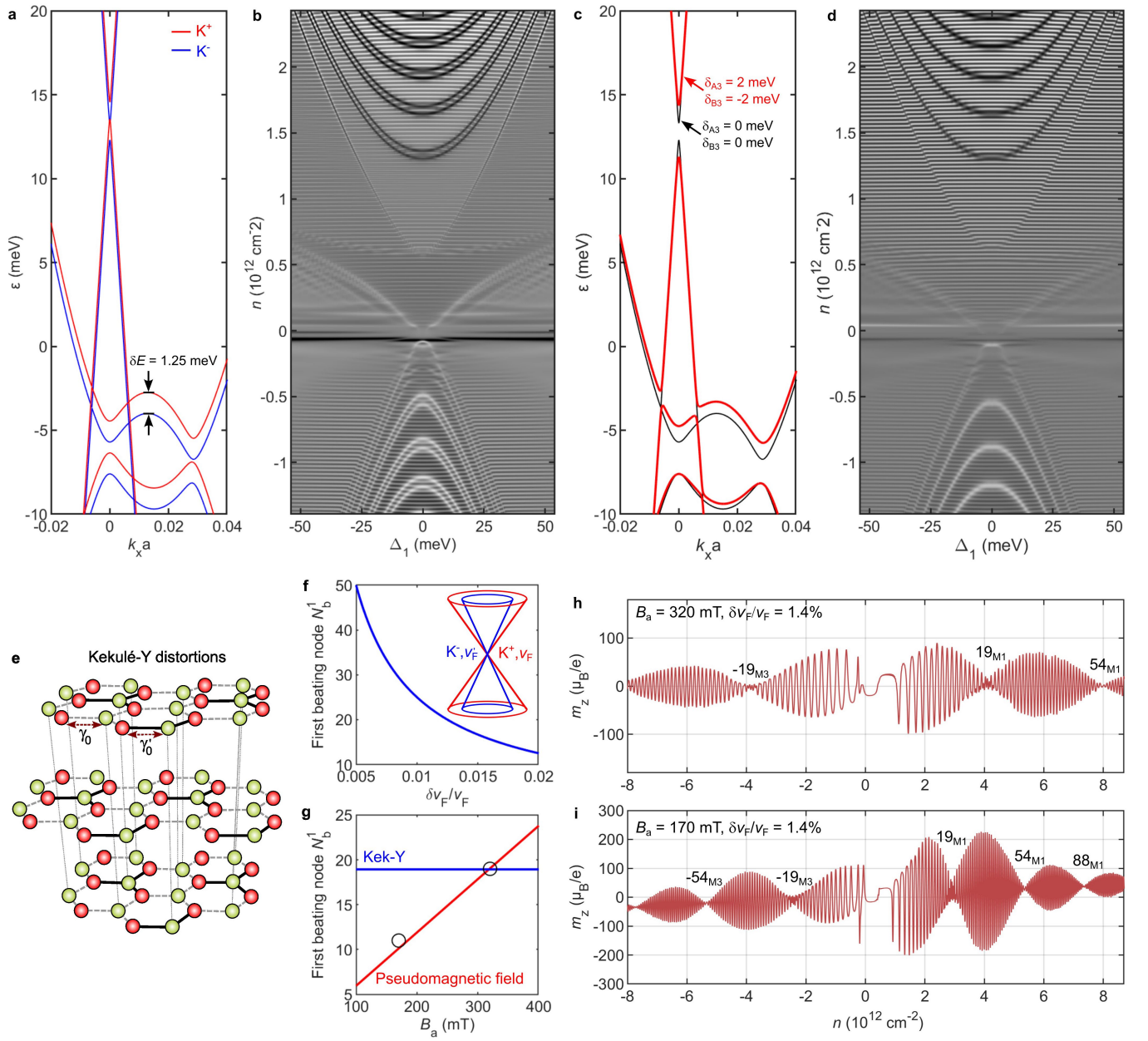

Extended Data Fig. 8 | Alternative mechanisms of LL interference. a, Band structure of ABA graphene with a relative energy shift of $\delta E = 1.25$ meV between the K^+ and K^- bands. **b**, The corresponding calculated QOs show splitting of the lowest MLG LLs inconsistent with the experimental data. **c**, Band structure of ABA graphene with (red) and without (black) staggered sublattice potential $\delta_{A3} = 2$ meV, $\delta_{B3} = -2$ meV. **d**, Corresponding calculated QOs showing no LL interference. **e**, Kekulé-Y distortion with γ_0' hopping parameter along the bonds emphasized in black. **f**, The dependence of the first beating node N_b^1 on the difference of the Fermi velocities $\Delta v_F/v_F$ of the two valleys. Inset, schematic of the MLG band dispersions of the two valleys. **g**, The dependence of N_b^1 on B_a for Kekulé-Y distortion (blue), PMF (red), and the experimental data (circles). **h**, The calculated QOs with $\Delta v_F/v_F = 1.4\%$ at $B_a = 320$ mT. **i**, Same as **h** at $B_a = 170$ mT.

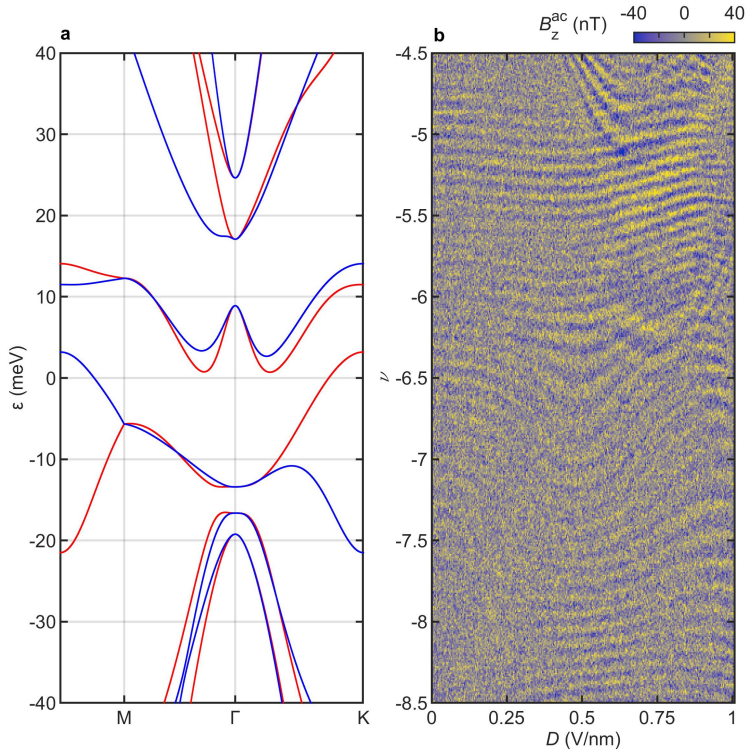

Extended Data Fig. 9 | Band structure and QOs in twisted double bilayer graphene (TDBLG). a, Calculated single-particle BS of TDBLG under an electrostatic potential difference of 30 meV, which causes an overlap between the valence flat and dispersive bands. **b**, QOs measured in TDBLG as a function of moiré filling factor ν and the displacement field *D* at 310 mT. The evolution of the flat and dispersive bands with *D* gives rise to very complicated QO patterns, which exemplifies the applicability of the dHvA technique to a broad range of vdW materials.

Extended Data Table 1 | Comparison of SWMc parameters in different works

Reference	γ_0	γ_1	γ_2	γ_3	γ_4	γ_5	δ	Δ_2	E_g^0
Taychatanapat, Nat. Phys. **7**, 621-625 (2011)	3160	390	-28	315	41	50	46	Nan	7
Shimazaki, arXiv: 1611.02395 (2016)	3100	390	-28	315	41	50	34	0	-5
Stepanov, PRL **117**, 076807 (2016)	3230	310	-32	300	40	10	27	1.8	6
Campos, PRL **117**, 066601 (2016)	3100	390	-18 ± 2	315	90 ± 50	10 ± 5	15 ± 3	>2.7	1
Datta, Nat. Commun. **8**, 14518 (2017)	3100	390	-28	Nan	Nan	10	21	Nan	2
Asakawa, PRL **119**, 186802 (2017)	3230	390	-23.7	315	43.8	6	14.3	Nan	-0.55
Datta, PRL **121**, 056801 (2018)	3100	390	-20	315	120	18	20	4.3	1
Zibrov, PRL **121**, 167601 (2018)	3100	380	-20	290	141	50	35.5	3.5	0.5
Che, PRL **125**, 246401 (2020) (suspended)	3100	355	-41	315	150	40	47	1	6.5
Che, PRL **125**, 246401 (2020) (*h*BN-aligned)	3100	355	-12.5	315	150	40	31.5	5.8	5.25
This work	3100	370 ± 10	-19 ± 0.5	315 ± 10	140 ± 15	20 ± 0.5	18.5 ± 0.5	3.8 ± 0.05	-1.0

The parameters are in units of meV.